Title
Generalized Lorentz-Lorenz homogenization formulas for binary lattice metamaterials

Journal
Physical Review B, 91(20)

ISSN
2469-9950

Authors
Sozio, Valentina
Vallecchi, Andrea
Albani, Matteo
et al.

Publication Date
2015-05-01

DOI
10.1103/physrevb.91.205127

Peer reviewed

Generalized Lorentz-Lorenz homogenization formulas for binary lattice metamaterials

Valentina Sozio,[1,*] Andrea Vallecchi,[2,†] Matteo Albani,[1,‡] and Filippo Capolino[3,§]
[1]*Department of Information Engineering and Mathematics, University of Siena, Siena, Italy*
[2]*Institute of Electronics, Communications and Information Technology, Queen's University Belfast, Belfast, United Kingdom*
[3]*Department of Electrical Engineering and Computer Science, University of California Irvine, Irvine, California 92697, USA*
(Received 5 November 2014; revised manuscript received 21 March 2015; published 22 May 2015)

Generalized Lorentz-Lorenz formulas are developed for the effective parameters of binary lattice metamaterials composed of a periodic arrangement of electric and/or magnetic inclusions. The proposed homogenization approach is based on a dual dipole approximation for the induced currents. The obtained formulas for the metamaterial effective electric and magnetic characteristics duly consider both electric and magnetic polarizabilities of the inclusions and completely describe the effects of frequency and spatial dispersion. Several numerical examples are provided to demonstrate the general applicability of the proposed formulas to different types of binary lattices and inclusions. It is shown that the proposed effective parameters have the capability of providing a physically sound and accurate description of wave propagation in the metamaterials in an extended range of frequencies in contrast to the equivalent parameters that can be defined in the absence of impressed sources and assuming a local anisotropic constitutive model, which hides inherent spatial dispersion effects and nonphysical features. To gain further insight into the metamaterial response and the physical meaningfulness of calculated effective parameters, the power flow of metamaterial supported modes is analyzed and its homogenized representation is compared to the complete description. A correspondence between the power flow due to the microscopic field and the effect of spatial dispersion in the homogenized parameters is established.

DOI: 10.1103/PhysRevB.91.205127 PACS number(s): 42.70.Qs, 78.20.−e, 42.25.Bs

I. INTRODUCTION

Metamaterials and plasmonics based on micro- and nanostructured metallic-dielectric composites are bringing an important revolution to the microwave and optics fields. In fact, metamaterials enable the realization of novel physical properties that are unattainable from natural materials. Examples of unconventional electromagnetic (EM) behaviors in such advanced materials include isotropic negative refraction, slow light, near-field enhancement with controlled polarization, as well as EM focusing and energy transfer that beats the diffraction limit. Such exotic artificial composite structures owe their peculiar properties both to the constituent materials, which comprise their elementary building blocks, and to their specific spatial arrangement.

Microwave and optical metamaterials rely on our understanding of EM-radiation-matter interaction, and the use of homogenization methods can provide a convenient characterization of such an interaction by describing metamaterials as bulk homogeneous materials with effective parameters that take into account their inherent qualities and complex nature, similarly to what is commonly done for natural materials and artificial composites with subwavelength granularity [1]. While the concept of homogenization theory easily applies to the asymptotic long-wavelength limit, e.g., the microwave regime where true subwavelength structures may be fabricated with ease, the optical regime challenges the underlying hypothesis of a true subwavelength unit cell. Indeed, for artificial materials the size of the lattice constant is typically only moderately smaller than the wavelength of light, in contrast to natural materials where the wavelength-to-lattice ratio is several orders of magnitude larger, even at optical frequencies. As a consequence, metamaterials can be characterized by non-negligible spatial dispersion effects [2].

A general approach to homogenize nonmagnetic periodic metamaterials has been recently introduced [3] that is capable of providing a comprehensive description of both spatial and frequency dispersion phenomena. This homogenization method is based on the Floquet representation of the field in periodic arrays and the introduction of a single generalized permittivity tensor that takes into account all the polarization effects, including artificial magnetism, bianisotropy, and higher-order spatial dispersion effects. Then, such a homogenization formalism has been applied to derive a generalization of the classical Lorentz-Lorenz formulas [4] for a dielectric crystal comprising of one particle per unit cell, in the hypothesis that particle interaction can be described by the dipolar terms only [5]. The Floquet-based homogenization approach developed in [3,5] has been subsequently generalized to the presence of electric and magnetic materials and arbitrary sources in the homogenization theory presented in [6], which explicitly takes into account weak spatial dispersion effects in the form of magnetoelectric coupling at the lattice level, thus ensuring the convergence to a local model in the long-wavelength limit. In [6] the unit cell is assumed to be sufficiently smaller than the operating wavelength to ensure that the induced microscopic polarization and magnetization vectors slowly vary within each unit cell. Upon this assumption, a Taylor expansion of the polarization and magnetization currents to derive a self-consistent definition of averaged fields is introduced, which is able to extract weak spatial dispersion effects and allows an averaged local description in the long-wavelength limit.

The aim of this paper is to extend the rigorous Floquet-based approach developed in [3,5,6] to the homogenization of binary

*valentina.sozio@unisi.it
†andrea.vallecchi@gmail.com
‡matteo.albani@dii.unisi.it
§f.capolino@uci.edu

lattice metamaterials composed of a periodic arrangement of electric and magnetic inclusions following the averaging scheme proposed in [6] that takes into account the complex wave interaction among inclusions, is independent of the form of excitation, and converges to a local model in the long-wavelength limit.

Indeed, the common approach to design a negative index metamaterial (NIM) is to combine a *magnetic* sublattice, exhibiting negative permeability, with an *electric* one, exhibiting negative permittivity [7]. At microwaves each sublattice consists of resonant metallic elements with different geometries, like for example split rings and wires, providing the magnetic and electric response, respectively. However, an alternative design route has been recently suggested that consists of exploiting the Mie resonances of individual scattering particles of less elaborate geometry, such as cylinders or spheres, made of electric or magnetic materials. This approach can be conveniently applied to generate a negative permittivity and/or permeability effect at infrared and optical frequencies, where such simpler structures can be realized and assembled by modern nanochemistry techniques [8], avoiding the use of the more expensive and complicated electron-beam lithography and focused ion-beam milling technique. Particularly, to address a three-dimensional (3D) isotropic NIM design, the use of spherical inclusions represents the most effective approach and provides the additional benefit of wide bandwidth at the electric and magnetic resonances due to the larger fraction of unit-cell volume that they can occupy [9]. This approach, based on the Mie resonances of spherical inclusions, has been recently applied by several authors to realize a NIM by combining two arrays composed of different types of spheres. The spheres can be either of the same dielectric material but of different size [10–12], or of different dielectric materials but of the same size [9]. In these designs, the relative permittivity and size of the two different spheres are chosen to have the first electric dipole resonant frequency of the larger spheres, or the spheres with the larger permittivity, coinciding with the first magnetic dipole resonant frequency of the smaller spheres, or the spheres with the smaller permittivity. As a result, the two sets of different dielectric spheres could together provide the electric and magnetic dipole moments of a single set of magnetodielectric spheres [13] with appreciable relative permittivity and permeability close to each other, and so enable the realization of an isotropic NIM inexpensively fabricated from purely dielectric spheres. A negative-index composite made of two interpenetrating lattices of polaritonic and metallic spheres has been also reported [14].

In the materials made up of a collection of such resonant particles, their combined scattering responses have been originally characterized by using the effective medium model formulated in [15], and considering the spheres resonate either in the first or second resonant modes of the Mie series, thus neglecting the electric polarizability of spheres in the magnetic resonant mode. Then, this formulation has been improved in [12] by taking into account also the electric polarizabilities of spheres operating in the magnetic resonant modes through a generalized form of the Clausius-Mossotti relation valid for a material with two types of inclusions having different electric polarizabilities [16].

These homogenization approaches do not properly take into account wave interaction among the inclusions and completely neglect the effect of spatial dispersion, thereby being sufficiently accurate only when the array period and the volume fraction of the inclusions are small, which is not the case for most metamaterials.

In [17,18] the dispersion diagrams for 3D arrays of two sets of dielectric and magnetodielectric spheres with certain specific unit cell configurations have been theoretically determined through the spherical modal analysis originally developed in [19], and the equivalent permittivity and permeability of the arrays have been deduced from the solution of the dispersion equation. However, this procedure, besides being restricted to two specific binary lattice configurations, still suffers from significant drawbacks because magnetoelectric coupling effects are embedded into the equivalent permittivity and permeability parameters as a form of weak spatial dispersion, such that the frequency dispersion of the equivalent parameters may contain nonphysical artifacts and not satisfy passivity, reciprocity, or other causality constraints typical of local parameters, as explained in detail in [6,20].

In this work we extend the generalized Lorentz-Lorenz (GLL) method proposed in [5] to the case when the unit cell of the periodic array contains more than one inclusion, for application to the homogenization of the class of binary lattice metamaterials, to which all the aforementioned NIM designs [9–14] belong. Based on the Floquet representation of the field in a periodic array used in optical crystals and further developed in [5,6] to describe the peculiar effects arising in periodic metamaterials, we develop a homogenization model for binary metamaterial arrays formed by spherical electric and magnetic particles that within a dipolar approximations for the induced current takes into account the complex wave interaction among inclusions. The proposed model provides a physically meaningful description of a wide class of binary metamaterials, valid even when the density of inclusions is not very small and classic homogenization models, like Clausius-Mossotti relations, lose their accuracy. Furthermore, this model properly takes into account weak forms of spatial dispersion in binary metamaterials and determines effective parameters that have local properties in the long-wavelength limit, differently from the equivalent parameters that, consistently with the terminology introduced in [6], can be defined in the absence of impressed sources upon the assumption of a local anisotropic constitutive model, and can only be used to describe the scattering properties of a metamaterial sample.

The paper has the following organization. In Sec. II the Floquet-based homogenization approach is generalized to the case when the unit cell of the periodic array contains more than one inclusion of electric and magnetic materials. In Sec. III closed-form expressions for the effective constitutive parameters are derived. In Sec. IV the effective parameters are applied to the solution of the dispersion equation. In Sec. V we analyze the homogenization model in the long-wavelength limit. Then, in Sec. VI, the relation between the effective parameters and the equivalent parameters defined upon the assumption of local anisotropic constitutive relations for the metamaterial and in the absence of impressed sources is provided. Section VII assesses the definition of the EM power

flow in the homogenized approach. Finally, Sec. VIII validates our model with numerical examples and further discussion.

II. FORMULATION

We consider a 3D periodic array consisting of a binary nanoparticle superlattice. The primitive vectors of the array are denoted by $\boldsymbol{a}_1$, $\boldsymbol{a}_2$, and $\boldsymbol{a}_3$, such that the unit cell volume is $V_{\text{cell}} = \boldsymbol{a}_1 \cdot (\boldsymbol{a}_2 \times \boldsymbol{a}_3)$. The reciprocal lattice is described by the vectors $\boldsymbol{b}_{1,2,3} = 2\pi(\boldsymbol{a}_{2,3,1} \times \boldsymbol{a}_{3,1,2})/V_{\text{cell}}$. The binary lattice consists of two types of inclusions that can be dielectric, magnetic, or conducting. To calculate the effective parameters of the array we follow the approach [6] and we assume the presence of impressed sources with arbitrary $e^{i\boldsymbol{k}\cdot\boldsymbol{r}}e^{-i\omega t}$ space and time harmonic dependence, uniformly distributed all over the array. As in [6] the microscopic fields $\boldsymbol{E}(\boldsymbol{r}), \boldsymbol{H}(\boldsymbol{r})$ satisfy Maxwell's equations

$$\begin{aligned} \nabla \times \boldsymbol{E}(\boldsymbol{r}) &= i\omega\mu_h \boldsymbol{H}(\boldsymbol{r}) + i\omega \boldsymbol{M}(\boldsymbol{r}) - \boldsymbol{K}_{\text{ext}} e^{i\boldsymbol{k}\cdot\boldsymbol{r}}, \\ \nabla \times \boldsymbol{H}(\boldsymbol{r}) &= -i\omega\varepsilon_h \boldsymbol{E}(\boldsymbol{r}) - i\omega \boldsymbol{P}(\boldsymbol{r}) + \boldsymbol{J}_{\text{ext}} e^{i\boldsymbol{k}\cdot\boldsymbol{r}}, \end{aligned} \tag{1}$$

where $\boldsymbol{J}_{\text{ext}} e^{i\boldsymbol{k}\cdot\boldsymbol{r}}$ and $\boldsymbol{K}_{\text{ext}} e^{i\boldsymbol{k}\cdot\boldsymbol{r}}$ are space harmonic electric and magnetic external current independently applied to the material, $\boldsymbol{P}(\boldsymbol{r})$ and $\boldsymbol{M}(\boldsymbol{r})$ are local polarization (including also conduction) and magnetization currents induced in the cell, and ε_h, μ_h are the host medium permittivity and permeability, respectively. In (1) the common time harmonic dependence $e^{-i\omega t}$ is suppressed. Because of spatial 3D periodicity, all fields can be expanded in Bragg modes, and in this work it is assumed that the averaged fields coincide with the corresponding fundamental harmonics providing the dominant contributions to the local fields

$$\boldsymbol{F}_{\text{av}} = \frac{1}{V_{\text{cell}}} \iiint_{\Omega} \boldsymbol{F}(\boldsymbol{r}) e^{-i\boldsymbol{k}\cdot\boldsymbol{r}} d^3\boldsymbol{r}, \tag{2}$$

where $\boldsymbol{F}$ denotes any field or current quantity and Ω is the metamaterial unit cell. In the Fourier domain, Maxwell's equations for the homogenized fields read as

$$\begin{aligned} i\boldsymbol{k} \times \boldsymbol{E}_{\text{av}} &= i\omega\mu_h \boldsymbol{H}_{\text{av}} + i\omega \boldsymbol{M}_{\text{av}} - \boldsymbol{K}_{\text{ext}}, \\ i\boldsymbol{k} \times \boldsymbol{H}_{\text{av}} &= -i\omega\varepsilon_h \boldsymbol{E}_{\text{av}} - i\omega \boldsymbol{P}_{\text{av}} + \boldsymbol{J}_{\text{ext}}. \end{aligned} \tag{3}$$

Generally this assumption would not provide an effective homogenized description of a metamaterial. Indeed, a main shortcoming of this approach could be that when the inclusions are formed by purely magnetic or dielectric materials the effective permittivity $\underline{\boldsymbol{\varepsilon}}_{\text{eff}}$ and permeability $\underline{\boldsymbol{\mu}}_{\text{eff}}$ would be equal to ε_h and μ_h, respectively, implying that artificial magnetic or electric polarization effects stemming from the rotation of electric or magnetic polarization, respectively, remain hidden as spatial dispersion effects in the tensors $\underline{\boldsymbol{\varepsilon}}_{\text{eff}}$ or $\underline{\boldsymbol{\mu}}_{\text{eff}}$. Specifically, we do not refer here to polarization currents associated with the resonances of individual inclusions (e.g., the circulating electric currents that can support the magnetic resonance of a nonmagnetic particle), which in our approach are completely subsumed into particle polarizabilities, as clarified in the following, but rather to other resonance effects possibly arising from currents induced across distinct particles in the metamaterial unit cell. In this regard, it must be noted that in contrast to other metamaterial structures that are engineered to force the electric field to circulate in the plane orthogonal to the incident magnetic field, providing an overall magnetic resonance (e.g., nanorings [21] and nanoclusters [22]), most binary lattices possess enough symmetries that higher order multipoles associated with polarization currents induced in different inclusions across the unit cell exactly vanish in the long wavelength limit. As a result, artificial magnetic effects stemming from the rotation of electric polarization currents across distinct particles in most binary lattices will be negligible with respect to the effective magnetic polarization induced at the level of each resonant inclusion. Similarly, the total electric polarization in the unit cell is mainly due to the electric polarizability of the inclusions.

Within the homogenization scheme above, we introduce a dipolar approximation and assume that the microscopic electric and magnetic current distributions in the unit cell can be described by a superposition of electric ($\boldsymbol{p}_e^n$, $n = 1,2$) and magnetic ($\boldsymbol{p}_m^n$, $n = 1,2$) dipole moments

$$\begin{aligned} \boldsymbol{P}(\boldsymbol{r}) &= \boldsymbol{p}_e^1 \delta(\boldsymbol{r} - \boldsymbol{r}_1) + \boldsymbol{p}_e^2 \delta(\boldsymbol{r} - \boldsymbol{r}_2), \\ \boldsymbol{M}(\boldsymbol{r}) &= \boldsymbol{p}_m^1 \delta(\boldsymbol{r} - \boldsymbol{r}_1) + \boldsymbol{p}_m^2 \delta(\boldsymbol{r} - \boldsymbol{r}_2), \end{aligned} \tag{4}$$

where $\boldsymbol{r}_n$, $n = 1,2$, denotes the position vector of the inclusion centres. Such a dual dipole approximation for the induced currents can be a good approximation when particle dimensions are much smaller than the wavelength in the host medium, and when the edge-to-edge spacing between spheres is larger than the radius of the spheres. Even for smaller distances this approximation can provide satisfactory results [22], though in general when spacing between the spheres becomes smaller than their radius, more accurate results may require taking into account also multipole field contributions. Moreover, we consider that the material is generally formed by bianisotropic particles. In such a case, the induced dipole moments can be related to the local fields as

$$\begin{aligned} \boldsymbol{p}_e^n &= \underline{\boldsymbol{\alpha}}_{ee}^n \varepsilon_h \cdot \boldsymbol{E}_{\text{loc}}(\boldsymbol{r}_n) + \underline{\boldsymbol{\alpha}}_{em}^n \sqrt{\varepsilon_h \mu_h} \cdot \boldsymbol{H}_{\text{loc}}(\boldsymbol{r}_n) \\ \boldsymbol{p}_m^n &= \underline{\boldsymbol{\alpha}}_{me}^n \sqrt{\varepsilon_h \mu_h} \cdot \boldsymbol{E}_{\text{loc}}(\boldsymbol{r}_n) + \underline{\boldsymbol{\alpha}}_{mm}^n \mu_h \cdot \boldsymbol{H}_{\text{loc}}(\boldsymbol{r}_n), \quad n = 1,2, \end{aligned} \tag{5}$$

where $\underline{\boldsymbol{\alpha}}_{ee}^n$, $\underline{\boldsymbol{\alpha}}_{em}^n$, $\underline{\boldsymbol{\alpha}}_{me}^n$, $\underline{\boldsymbol{\alpha}}_{mm}^n$ ($n = 1,2$) are the electric, electromagnetic, magnetoelectric, and magnetic polarizability dyadics, respectively; all of which have dimensions of a volume. The local field at each particle position can be expressed as

$$\begin{aligned} \boldsymbol{E}_{\text{loc}}(\boldsymbol{r}_n) &= \boldsymbol{E}_{\text{ext}} e^{i\boldsymbol{k}\cdot\boldsymbol{r}_n} + \boldsymbol{E}_s(\boldsymbol{r}_n), \\ \boldsymbol{H}_{\text{loc}}(\boldsymbol{r}_n) &= \boldsymbol{H}_{\text{ext}} e^{i\boldsymbol{k}\cdot\boldsymbol{r}_n} + \boldsymbol{H}_s(\boldsymbol{r}_n), \end{aligned} \tag{6}$$

where $\boldsymbol{E}_{\text{ext}}$, $\boldsymbol{H}_{\text{ext}}$ denote the space harmonic field radiated by the external sources as if the metamaterial inclusions were not present (incident field), i.e., in the unbounded homogeneous background material, satisfying

$$\begin{aligned} i\boldsymbol{k} \times \boldsymbol{E}_{\text{ext}} &= i\omega\mu_h \boldsymbol{H}_{\text{ext}} - \boldsymbol{K}_{\text{ext}}, \\ i\boldsymbol{k} \times \boldsymbol{H}_{\text{ext}} &= -i\omega\varepsilon_h \boldsymbol{E}_{\text{ext}} + \boldsymbol{J}_{\text{ext}}, \end{aligned} \tag{7}$$

and $\boldsymbol{E}_s(\boldsymbol{r}_n)$, $\boldsymbol{H}_s(\boldsymbol{r}_n)$ are the induced fields scattered from the array except the inclusion at $\boldsymbol{r}_n$. $\boldsymbol{E}_s(\boldsymbol{r}_n)$, $\boldsymbol{H}_s(\boldsymbol{r}_n)$ can be expressed in terms of the 3D array dyadic Green's functions

as

$$\begin{aligned}\boldsymbol{E}_s(\boldsymbol{r}_n) &= \boldsymbol{E}_{s,\mathrm{av}}e^{i\boldsymbol{k}\cdot\boldsymbol{r}_n} + \sum_{\ell=1}^{2}\frac{1}{\varepsilon_h}\underline{\boldsymbol{C}}_{\mathrm{int}}(\boldsymbol{r}_n-\boldsymbol{r}_\ell)\cdot\boldsymbol{p}_e^\ell \\ &\quad + \sum_{\ell=1}^{2}\frac{1}{\sqrt{\varepsilon_h\mu_h}}\underline{\boldsymbol{C}}_{e,m}(\boldsymbol{r}_n-\boldsymbol{r}_\ell)\cdot\boldsymbol{p}_m^\ell, \\ \boldsymbol{H}_s(\boldsymbol{r}_n) &= \boldsymbol{H}_{s,\mathrm{av}}e^{i\boldsymbol{k}\cdot\boldsymbol{r}_n} - \sum_{\ell=1}^{2}\frac{1}{\sqrt{\varepsilon_h\mu_h}}\underline{\boldsymbol{C}}_{e,m}(\boldsymbol{r}_n-\boldsymbol{r}_\ell)\cdot\boldsymbol{p}_e^\ell \\ &\quad + \sum_{\ell=1}^{2}\frac{1}{\mu_h}\underline{\boldsymbol{C}}_{\mathrm{int}}(\boldsymbol{r}_n-\boldsymbol{r}_\ell)\cdot\boldsymbol{p}_m^\ell, \end{aligned} \tag{8}$$

where $\boldsymbol{E}_{s,\mathrm{av}}$, $\boldsymbol{H}_{s,\mathrm{av}}$ represent the contribution of the field scattered by the inclusions to the average electric and magnetic fields, and the dyadic regularized (both in space and spectrum) Green's functions [3,5] are defined as

$$\begin{aligned}\underline{\boldsymbol{C}}_{\mathrm{int}}(\boldsymbol{r}-\boldsymbol{r}') &= \left[k_h^2\underline{\boldsymbol{I}} + \nabla\nabla\right]\Phi_{\mathrm{reg}}(\boldsymbol{r}-\boldsymbol{r}'), \\ \underline{\boldsymbol{C}}_{e,m}(\boldsymbol{r}-\boldsymbol{r}') &= \frac{i}{k_h}\nabla\times\underline{\boldsymbol{C}}_{\mathrm{int}}(\boldsymbol{r}-\boldsymbol{r}') = ik_h\nabla\times\underline{\boldsymbol{I}}\Phi_{\mathrm{reg}}(\boldsymbol{r}-\boldsymbol{r}'), \end{aligned} \tag{9}$$

in which $k_h=\omega\sqrt{\varepsilon_h\mu_h}$ is the host medium wave number, and Φ_{reg} is the regularized scalar Green's function

$$\Phi_{\mathrm{reg}}(\boldsymbol{r}-\boldsymbol{r}') = \begin{cases}\Phi_p(\boldsymbol{r}-\boldsymbol{r}') - \Phi_{\mathrm{av}}e^{i\boldsymbol{k}\cdot(\boldsymbol{r}-\boldsymbol{r}')} & \text{if } \boldsymbol{r}\neq\boldsymbol{r}', \\ \Phi_p(\boldsymbol{r}-\boldsymbol{r}') - \Phi_{\mathrm{av}}e^{i\boldsymbol{k}\cdot(\boldsymbol{r}-\boldsymbol{r}')} - \Phi_f(\boldsymbol{r}-\boldsymbol{r}') & \text{if } \boldsymbol{r}=\boldsymbol{r}', \end{cases} \tag{10}$$

with

$$\Phi_{\mathrm{av}} = \frac{1}{V_{\mathrm{cell}}}\frac{1}{\boldsymbol{k}\cdot\boldsymbol{k}-k_h^2}, \quad \Phi_f(\boldsymbol{r}-\boldsymbol{r}') = \frac{e^{ik_h|\boldsymbol{r}-\boldsymbol{r}'|}}{4\pi|\boldsymbol{r}-\boldsymbol{r}'|}, \tag{11}$$

and

$$\Phi_p(\boldsymbol{r}) = \sum_{\boldsymbol{I}}\Phi_f(\boldsymbol{r}-\boldsymbol{r}_{\boldsymbol{I}},\omega)e^{i\boldsymbol{k}\cdot\boldsymbol{r}_{\boldsymbol{I}}} = \frac{1}{V_{\mathrm{cell}}}\sum_{\boldsymbol{I}}\frac{e^{i\boldsymbol{k}_{\boldsymbol{I}}\cdot\boldsymbol{r}}}{\boldsymbol{k}_{\boldsymbol{I}}\cdot\boldsymbol{k}_{\boldsymbol{I}}-k_h^2}. \tag{12}$$

The latter is the crystal periodic scalar Green's function, i.e., the field produced by an array of point sources located at lattice point positions $\boldsymbol{r}_{\boldsymbol{I}}=p_1\boldsymbol{a}_1+p_2\boldsymbol{a}_2+p_3\boldsymbol{a}_3$ (with spatial density $1/V_{\mathrm{cell}}$), with $\boldsymbol{I}=(p_1,p_2,p_3)$ a triple index of integers, and excited with the imposed phase progression $e^{i\boldsymbol{k}\cdot\boldsymbol{r}_{\boldsymbol{I}}}$. Such a scalar periodic Green's function is regularized in space when evaluated at $\boldsymbol{r}=\boldsymbol{r}'$, by extracting the free-space component $\Phi_f(\boldsymbol{r}-\boldsymbol{r}')$ [i.e., the $\boldsymbol{I}=(0,0,0)$ contribution], not to include the contribution of the particle $\ell=n$ at $\boldsymbol{r}_n$ when evaluating the field at $\boldsymbol{r}_n$, as prescribed by the local field definition, but only the contributions corresponding to the particles in the same position in all the other cells as in the reference one. In addition, the scalar periodic Green's function, which also admits a discrete spectral representation in terms of Bragg's space harmonic waves with wave numbers $\boldsymbol{k}_{\boldsymbol{I}}=q_1\boldsymbol{b}_1+q_2\boldsymbol{b}_2+q_3\boldsymbol{b}_3+\boldsymbol{k}$, with $\boldsymbol{I}=(q_1,q_2,q_3)$ a triple index of integers, is regularized in the spectral (wave number) domain at $\boldsymbol{k}\cdot\boldsymbol{k}=k_h^2$, by extracting the $\boldsymbol{I}=(0,0,0)$ $\boldsymbol{k}_{000}=\boldsymbol{k}$ Bragg's harmonic corresponding to the homogenized average field. Such terms appear explicitly in (8) as the first terms on the right-hand side:

$$\begin{aligned}\boldsymbol{E}_{s,\mathrm{av}} &= \frac{1}{V_{\mathrm{cell}}}\frac{1}{\boldsymbol{k}\cdot\boldsymbol{k}-k_h^2}\left\{\frac{1}{\varepsilon_h}\left[k_h^2\underline{\boldsymbol{I}}-\boldsymbol{k}\boldsymbol{k}\right]\cdot\sum_{\ell=1}^{2}\boldsymbol{p}_e^\ell e^{-i\boldsymbol{k}\cdot\boldsymbol{r}_\ell} - \omega\boldsymbol{k}\times\underline{\boldsymbol{I}}\cdot\sum_{\ell=1}^{2}\boldsymbol{p}_m^\ell e^{-i\boldsymbol{k}\cdot\boldsymbol{r}_\ell}\right\}, \\ \boldsymbol{H}_{s,\mathrm{av}} &= \frac{1}{V_{\mathrm{cell}}}\frac{1}{\boldsymbol{k}\cdot\boldsymbol{k}-k_h^2}\left\{\omega\boldsymbol{k}\times\underline{\boldsymbol{I}}\cdot\sum_{\ell=1}^{2}\boldsymbol{p}_e^\ell e^{-i\boldsymbol{k}\cdot\boldsymbol{r}_\ell} + \frac{1}{\mu_h}\left[k_h^2\underline{\boldsymbol{I}}-\boldsymbol{k}\boldsymbol{k}\right]\cdot\sum_{\ell=1}^{2}\boldsymbol{p}_m^\ell e^{-i\boldsymbol{k}\cdot\boldsymbol{r}_\ell}\right\}. \end{aligned} \tag{13}$$

The remaining part of the particle scattered field in (8) is therefore the fluctuation of the microscopic field in addition to its macroscopic average.

III. EFFECTIVE PARAMETERS

Substituting (8) into (6) and expressing the local fields $\boldsymbol{E}_{\mathrm{loc}}$, $\boldsymbol{H}_{\mathrm{loc}}$ by means of (5) provides a linear system that can be solved to obtain the explicit expressions of the particle dipole moments:

$$\begin{aligned}&\sum_{\ell=1}^{2}\left[\underline{\boldsymbol{I}}\delta_{n\ell} - \underline{\boldsymbol{\alpha}}_{ee}^n\underline{\boldsymbol{C}}_{\mathrm{int}}(\boldsymbol{r}_n-\boldsymbol{r}_\ell) + \underline{\boldsymbol{\alpha}}_{em}^n\underline{\boldsymbol{C}}_{e,m}(\boldsymbol{r}_n-\boldsymbol{r}_\ell)\right]\cdot\boldsymbol{p}_e^\ell + \sqrt{\frac{\varepsilon_h}{\mu_h}}\sum_{\ell=1}^{2}\left[-\underline{\boldsymbol{\alpha}}_{ee}^n\underline{\boldsymbol{C}}_{e,m}(\boldsymbol{r}_n-\boldsymbol{r}_\ell) - \underline{\boldsymbol{\alpha}}_{em}^n\underline{\boldsymbol{C}}_{\mathrm{int}}(\boldsymbol{r}_n-\boldsymbol{r}_\ell)\right]\cdot\boldsymbol{p}_m^\ell \\ &\quad = \varepsilon_h\left[\underline{\boldsymbol{\alpha}}_{ee}^n\cdot(\boldsymbol{E}_{\mathrm{ext}}+\boldsymbol{E}_{s,\mathrm{av}}) + \sqrt{\frac{\mu_h}{\varepsilon_h}}\underline{\boldsymbol{\alpha}}_{em}^n\cdot(\boldsymbol{H}_{\mathrm{ext}}+\boldsymbol{H}_{s,\mathrm{av}})\right]e^{i\boldsymbol{k}\cdot\boldsymbol{r}_n}, \end{aligned}$$

$$\sum_{\ell=1}^{2}\sqrt{\frac{\mu_h}{\varepsilon_h}}\left[-\underline{\boldsymbol{\alpha}}^n_{me}\underline{\boldsymbol{C}}_{\rm int}(\boldsymbol{r}_n-\boldsymbol{r}_\ell)+\underline{\boldsymbol{\alpha}}^n_{mm}\underline{\boldsymbol{C}}_{e,m}(\boldsymbol{r}_n-\boldsymbol{r}_\ell)\right]\cdot\boldsymbol{p}^\ell_e+\sum_{\ell=1}^{2}\left[\underline{\boldsymbol{I}}\delta_{n\ell}-\underline{\boldsymbol{\alpha}}^n_{me}\underline{\boldsymbol{C}}_{e,m}(\boldsymbol{r}_n-\boldsymbol{r}_\ell)-\underline{\boldsymbol{\alpha}}^n_{mm}\underline{\boldsymbol{C}}_{\rm int}(\boldsymbol{r}_n-\boldsymbol{r}_\ell)\right]\cdot\boldsymbol{p}^\ell_m$$
$$=\mu_h\left[\sqrt{\frac{\varepsilon_h}{\mu_h}}\underline{\boldsymbol{\alpha}}^n_{me}\cdot(\boldsymbol{E}_{\rm ext}+\boldsymbol{E}_{s,\rm av})+\underline{\boldsymbol{\alpha}}^n_{mm}\cdot(\boldsymbol{H}_{\rm ext}+\boldsymbol{H}_{s,\rm av})\right]e^{i\boldsymbol{k}\cdot\boldsymbol{r}_n},\tag{14}$$

with $n=1,2$. The above linear system is recast in the following matrix block form:

$$\begin{bmatrix}\underline{\boldsymbol{I}}\delta_{n\ell}-\underline{\boldsymbol{\alpha}}^n_{ee}\underline{\boldsymbol{C}}_{\rm int}(\boldsymbol{r}_n-\boldsymbol{r}_\ell)+\underline{\boldsymbol{\alpha}}^n_{em}\underline{\boldsymbol{C}}_{e,m}(\boldsymbol{r}_n-\boldsymbol{r}_\ell) & -\underline{\boldsymbol{\alpha}}^n_{ee}\underline{\boldsymbol{C}}_{e,m}(\boldsymbol{r}_n-\boldsymbol{r}_\ell)-\underline{\boldsymbol{\alpha}}^n_{em}\underline{\boldsymbol{C}}_{\rm int}(\boldsymbol{r}_n-\boldsymbol{r}_\ell)\\ -\underline{\boldsymbol{\alpha}}^n_{me}\underline{\boldsymbol{C}}_{\rm int}(\boldsymbol{r}_n-\boldsymbol{r}_\ell)+\underline{\boldsymbol{\alpha}}^n_{mm}\underline{\boldsymbol{C}}_{e,m}(\boldsymbol{r}_n-\boldsymbol{r}_\ell) & \underline{\boldsymbol{I}}\delta_{n\ell}-\underline{\boldsymbol{\alpha}}^n_{me}\underline{\boldsymbol{C}}_{e,m}(\boldsymbol{r}_n-\boldsymbol{r}_\ell)-\underline{\boldsymbol{\alpha}}^n_{mm}\underline{\boldsymbol{C}}_{\rm int}(\boldsymbol{r}_n-\boldsymbol{r}_\ell)\end{bmatrix}_{12\times12}\cdot\begin{bmatrix}\boldsymbol{p}^\ell_e\\ \varepsilon_h\\ \boldsymbol{p}^\ell_m\\ \sqrt{\varepsilon_h\mu_h}\end{bmatrix}_{12\times1}$$
$$=\begin{bmatrix}\underline{\boldsymbol{\alpha}}^n_{ee}e^{i\boldsymbol{k}\cdot\boldsymbol{r}_n} & \underline{\boldsymbol{\alpha}}^n_{em}e^{i\boldsymbol{k}\cdot\boldsymbol{r}_n}\\ \underline{\boldsymbol{\alpha}}^n_{me}e^{i\boldsymbol{k}\cdot\boldsymbol{r}_n} & \underline{\boldsymbol{\alpha}}^n_{mm}e^{i\boldsymbol{k}\cdot\boldsymbol{r}_n}\end{bmatrix}_{12\times6}\cdot\begin{bmatrix}\boldsymbol{E}_{\rm av}\\ \zeta_h\boldsymbol{H}_{\rm av}\end{bmatrix}_{6\times1},\tag{15}$$

where indices (n,ℓ), correspond to the 3×3 dyadic coefficients describing the contribution to the microscopic field at $\boldsymbol{r}_n$ of the ℓth electric and magnetic dipoles arranged along the rows and columns of the system matrix, respectively, and we have introduced the vectors $\boldsymbol{E}_{\rm av},\boldsymbol{H}_{\rm av}$ corresponding to the total average fields

$$\boldsymbol{E}_{\rm av}=\boldsymbol{E}_{\rm ext}+\boldsymbol{E}_{s,\rm av},\quad \boldsymbol{H}_{\rm av}=\boldsymbol{H}_{\rm ext}+\boldsymbol{H}_{s,\rm av}.\tag{16}$$

Then the induced electric and magnetic dipoles can be expressed as

$$\begin{bmatrix}\boldsymbol{p}^\ell_e\\ \varepsilon_h\\ \boldsymbol{p}^\ell_m\\ \sqrt{\varepsilon_h\mu_h}\end{bmatrix}_{12\times1}=\begin{bmatrix}\underline{\boldsymbol{A}}^{\ell n}_{ee} & \underline{\boldsymbol{A}}^{\ell n}_{em}\\ \underline{\boldsymbol{A}}^{\ell n}_{me} & \underline{\boldsymbol{A}}^{\ell n}_{mm}\end{bmatrix}_{12\times12}\cdot\begin{bmatrix}\underline{\boldsymbol{\alpha}}^n_{ee}e^{i\boldsymbol{k}\cdot\boldsymbol{r}_n} & \underline{\boldsymbol{\alpha}}^n_{em}e^{i\boldsymbol{k}\cdot\boldsymbol{r}_n}\\ \underline{\boldsymbol{\alpha}}^n_{me}e^{i\boldsymbol{k}\cdot\boldsymbol{r}_n} & \underline{\boldsymbol{\alpha}}^n_{mm}e^{i\boldsymbol{k}\cdot\boldsymbol{r}_n}\end{bmatrix}_{12\times6}\cdot\begin{bmatrix}\boldsymbol{E}_{\rm av}\\ \zeta_h\boldsymbol{H}_{\rm av}\end{bmatrix}_{6\times1},\tag{17}$$

where

$$\begin{bmatrix}\underline{\boldsymbol{A}}^{\ell n}_{ee} & \underline{\boldsymbol{A}}^{\ell n}_{em}\\ \underline{\boldsymbol{A}}^{\ell n}_{me} & \underline{\boldsymbol{A}}^{\ell n}_{mm}\end{bmatrix}_{12\times12}=\begin{bmatrix}\underline{\boldsymbol{I}}\delta_{n\ell}-\underline{\boldsymbol{\alpha}}^n_{ee}\underline{\boldsymbol{C}}_{\rm int}(\boldsymbol{r}_n-\boldsymbol{r}_\ell)+\underline{\boldsymbol{\alpha}}^n_{em}\underline{\boldsymbol{C}}_{e,m}(\boldsymbol{r}_n-\boldsymbol{r}_\ell) & -\underline{\boldsymbol{\alpha}}^n_{ee}\underline{\boldsymbol{C}}_{e,m}(\boldsymbol{r}_n-\boldsymbol{r}_\ell)-\underline{\boldsymbol{\alpha}}^n_{em}\underline{\boldsymbol{C}}_{\rm int}(\boldsymbol{r}_n-\boldsymbol{r}_\ell)\\ -\underline{\boldsymbol{\alpha}}^n_{me}\underline{\boldsymbol{C}}_{\rm int}(\boldsymbol{r}_n-\boldsymbol{r}_\ell)+\underline{\boldsymbol{\alpha}}^n_{mm}\underline{\boldsymbol{C}}_{e,m}(\boldsymbol{r}_n-\boldsymbol{r}_\ell) & \underline{\boldsymbol{I}}\delta_{n\ell}-\underline{\boldsymbol{\alpha}}^n_{me}\underline{\boldsymbol{C}}_{e,m}(\boldsymbol{r}_n-\boldsymbol{r}_\ell)-\underline{\boldsymbol{\alpha}}^n_{mm}\underline{\boldsymbol{C}}_{\rm int}(\boldsymbol{r}_n-\boldsymbol{r}_\ell)\end{bmatrix}^{-1}_{12\times12}.\tag{18}$$

As anticipated in Sec. II, most binary lattices, e.g., body and face centered cubic (bcc and fcc) lattices, and hexagonal lattices, possess enough symmetries that higher order multipoles associated with the polarization currents induced in distinct inclusions exactly vanish in the long wavelength limit when $\boldsymbol{k}\to0$. As a result, the artificial magnetic effect stemming from electric polarization currents in distinct inclusions assuming a circulating pattern is generally much weaker than the magnetic polarization induced in the resonant electric or magnetic inclusions and described by $\underline{\boldsymbol{\alpha}}^n_{mm}$, at least for moderate values of $\boldsymbol{k}$. In other words, the magnetic response of a binary metamaterial essentially arises from the magnetic resonance of individual particles that within the adopted dual dipole approximation is incorporated into a resonant magnetic polarizability. This is the reason why a distinction is made between magnetic resonance of individual inclusions and other magnetic effects possibly associated with the induced current distributions across distinct particles. Analogously the total electric polarization in the unit cell is mainly due to the electric polarizability of the inclusions while the circulating magnetic polarizability contribution to it is negligible. For similar reasons, both the electric and magnetic quadrupole moments in the unit cell, possibly supported by the distribution of the polarization currents across distinct inclusions, are also usually negligible.

Upon the above considerations, the distributions of $\boldsymbol{P}(\boldsymbol{r})$ and $\boldsymbol{M}(\boldsymbol{r})$ are described exclusively in terms of electric and magnetic dipole moments and we write the constitutive model relating averaged displacement vectors in the form [6]

$$\boldsymbol{D}_{\rm av}=\varepsilon_h\boldsymbol{E}_{\rm av}+\boldsymbol{P}_{\rm av},\quad \boldsymbol{B}_{\rm av}=\mu_h\boldsymbol{H}_{\rm av}+\boldsymbol{M}_{\rm av},\tag{19}$$

where average polarization and magnetization are defined, according to (2), as

$$\boldsymbol{P}_{\rm av}=\frac{1}{V_{\rm cell}}\int_\Omega\boldsymbol{P}(\boldsymbol{r})e^{-i\boldsymbol{k}\cdot\boldsymbol{r}}d^3\boldsymbol{r}=\frac{1}{V_{\rm cell}}\sum_{\ell=1}^{2}\boldsymbol{p}^\ell_e e^{-i\boldsymbol{k}\cdot\boldsymbol{r}_\ell},$$
$$\boldsymbol{M}_{\rm av}=\frac{1}{V_{\rm cell}}\int_\Omega\boldsymbol{M}(\boldsymbol{r})e^{-i\boldsymbol{k}\cdot\boldsymbol{r}}d^3\boldsymbol{r}=\frac{1}{V_{\rm cell}}\sum_{\ell=1}^{2}\boldsymbol{p}^\ell_m e^{-i\boldsymbol{k}\cdot\boldsymbol{r}_\ell}.\tag{20}$$

Substituting (17) into (20) yields

$$\boldsymbol{P}_{\rm av}=\frac{\varepsilon_h}{V_{\rm cell}}\sum_{\ell,n=1}^{2}\left(\underline{\boldsymbol{A}}^{\ell n}_{ee}\underline{\boldsymbol{\alpha}}^n_{ee}+\underline{\boldsymbol{A}}^{\ell n}_{em}\underline{\boldsymbol{\alpha}}^n_{me}\right)e^{i\boldsymbol{k}\cdot(\boldsymbol{r}_n-\boldsymbol{r}_\ell)}\cdot\boldsymbol{E}_{\rm av}$$
$$+\frac{\sqrt{\varepsilon_h\mu_h}}{V_{\rm cell}}\sum_{\ell,n=1}^{2}\left(\underline{\boldsymbol{A}}^{\ell n}_{ee}\underline{\boldsymbol{\alpha}}^n_{em}+\underline{\boldsymbol{A}}^{\ell n}_{em}\underline{\boldsymbol{\alpha}}^n_{mm}\right)e^{i\boldsymbol{k}\cdot(\boldsymbol{r}_n-\boldsymbol{r}_\ell)}\cdot\boldsymbol{H}_{\rm av},$$

$$\boldsymbol{M}_{\rm av} = \frac{\sqrt{\varepsilon_h\mu_h}}{V_{\rm cell}} \sum_{\ell,n=1}^{2} \left(\underline{\boldsymbol{A}}_{me}^{\ell n}\underline{\boldsymbol{\alpha}}_{ee}^{n} + \underline{\boldsymbol{A}}_{mm}^{\ell n}\underline{\boldsymbol{\alpha}}_{me}^{n}\right) e^{i\boldsymbol{k}\cdot(\boldsymbol{r}_n-\boldsymbol{r}_\ell)} \cdot \boldsymbol{E}_{\rm av} + \frac{\mu_h}{V_{\rm cell}} \sum_{\ell,n=1}^{2} \left(\underline{\boldsymbol{A}}_{me}^{\ell n}\underline{\boldsymbol{\alpha}}_{em}^{n} + \underline{\boldsymbol{A}}_{mm}^{\ell n}\underline{\boldsymbol{\alpha}}_{mm}^{n}\right) e^{i\boldsymbol{k}\cdot(\boldsymbol{r}_n-\boldsymbol{r}_\ell)} \cdot \boldsymbol{H}_{\rm av}, \tag{21}$$

and comparing (19) to the constitutive relations for a bianisotropic material

$$\begin{aligned} \boldsymbol{D}_{\rm av} &= \underline{\boldsymbol{\varepsilon}}_{\rm eff} \cdot \boldsymbol{E}_{\rm av} + \underline{\boldsymbol{\xi}}_{\rm eff} \cdot \boldsymbol{H}_{\rm av}, \\ \boldsymbol{B}_{\rm av} &= \underline{\boldsymbol{\mu}}_{\rm eff} \cdot \boldsymbol{H}_{\rm av} + \underline{\boldsymbol{\zeta}}_{\rm eff} \cdot \boldsymbol{E}_{\rm av}, \end{aligned} \tag{22}$$

we obtain the following expressions for the effective parameters of a binary metamaterial:

$$\begin{aligned} \underline{\boldsymbol{\varepsilon}}_{\rm eff} &= \varepsilon_h \left[\underline{\boldsymbol{I}} + \frac{1}{V_{\rm cell}} \sum_{\ell,n=1}^{2} \left(\underline{\boldsymbol{A}}_{ee}^{\ell n}\underline{\boldsymbol{\alpha}}_{ee}^{n} + \underline{\boldsymbol{A}}_{em}^{\ell n}\underline{\boldsymbol{\alpha}}_{me}^{n}\right) e^{i\boldsymbol{k}\cdot(\boldsymbol{r}_n-\boldsymbol{r}_\ell)}\right], \\ \underline{\boldsymbol{\mu}}_{\rm eff} &= \mu_h \left[\underline{\boldsymbol{I}} + \frac{1}{V_{\rm cell}} \sum_{\ell,n=1}^{2} \left(\underline{\boldsymbol{A}}_{me}^{\ell n}\underline{\boldsymbol{\alpha}}_{em}^{n} + \underline{\boldsymbol{A}}_{mm}^{\ell n}\underline{\boldsymbol{\alpha}}_{mm}^{n}\right) e^{i\boldsymbol{k}\cdot(\boldsymbol{r}_n-\boldsymbol{r}_\ell)}\right], \\ \underline{\boldsymbol{\xi}}_{\rm eff} &= \sqrt{\varepsilon_h\mu_h}\,\frac{1}{V_{\rm cell}} \sum_{\ell,n=1}^{2} \left(\underline{\boldsymbol{A}}_{ee}^{\ell n}\underline{\boldsymbol{\alpha}}_{em}^{n} + \underline{\boldsymbol{A}}_{em}^{\ell n}\underline{\boldsymbol{\alpha}}_{mm}^{n}\right) e^{i\boldsymbol{k}\cdot(\boldsymbol{r}_n-\boldsymbol{r}_\ell)}, \\ \underline{\boldsymbol{\zeta}}_{\rm eff} &= \sqrt{\varepsilon_h\mu_h}\,\frac{1}{V_{\rm cell}} \sum_{\ell,n=1}^{2} \left(\underline{\boldsymbol{A}}_{me}^{\ell n}\underline{\boldsymbol{\alpha}}_{ee}^{n} + \underline{\boldsymbol{A}}_{mm}^{\ell n}\underline{\boldsymbol{\alpha}}_{me}^{n}\right) e^{i\boldsymbol{k}\cdot(\boldsymbol{r}_n-\boldsymbol{r}_\ell)}. \end{aligned} \tag{23}$$

The closed form expressions (23) with (18) provide the effective constitutive parameters of a binary metamaterial valid for any pair $(\omega,\boldsymbol{k})$ and arbitrary electric and/or magnetic excitation, thereby this homogenized description does not depend on the specific impressed field distribution in each unit cell but instead represents the inherent response of the metamaterial as a bulk. The first two relations in (23) represent closed form expressions for the effective permittivity and permeability of a binary metamaterial that generalize the Clausius-Mossotti homogenization formulas [16] by rigorously taking into account the coupling among the inclusions and their polarization properties. It can also be observed that the presence of magnetoelectric coupling is described by the bianisotropy parameters $\underline{\boldsymbol{\xi}}_{\rm eff}$ and $\underline{\boldsymbol{\zeta}}_{\rm eff}$. Indeed these parameters comprise two contributions: one is associated with magnetoelectric effects at the inclusion level, which are incorporated in the model through the electromagnetic and magnetoelectric polarizabilities $\underline{\boldsymbol{\alpha}}_{me}^{n}$, $\underline{\boldsymbol{\alpha}}_{em}^{n}$, $n = 1,2$; the other one is associated with inherent magnetoelectric coupling effects arising at the lattice level and taken into account by $\underline{\boldsymbol{C}}_{e,m}$. It can be verified that for reciprocal inclusions, such that $\underline{\boldsymbol{\alpha}}_{ee}^{n} = [\underline{\boldsymbol{\alpha}}_{ee}^{n}]^t$ and $\underline{\boldsymbol{\alpha}}_{mm}^{n} = [\underline{\boldsymbol{\alpha}}_{mm}^{n}]^t$ are symmetric and $\underline{\boldsymbol{\alpha}}_{em}^{n} = -[\underline{\boldsymbol{\alpha}}_{me}^{n}]^t$, due to the different symmetries with respect to $\boldsymbol{k}$ of the regularized dyadic Green's functions $\underline{\boldsymbol{C}}_{\rm int}(\boldsymbol{k}) = [\underline{\boldsymbol{C}}_{\rm int}(-\boldsymbol{k})]^t$ and $\underline{\boldsymbol{C}}_{e,m}(\boldsymbol{k}) = -[\underline{\boldsymbol{C}}_{e,m}(-\boldsymbol{k})]^t$, the constitutive relations defined in (23) with (18) satisfy the reciprocity property $\underline{\varepsilon}_{\rm eff}(\boldsymbol{k}) = [\underline{\varepsilon}_{\rm eff}(-\boldsymbol{k})]^t$, $\underline{\mu}_{\rm eff}(\boldsymbol{k}) = [\underline{\mu}_{\rm eff}(-\boldsymbol{k})]^t$, and $\underline{\boldsymbol{\zeta}}_{\rm eff}(\boldsymbol{k}) = -[\underline{\boldsymbol{\xi}}_{\rm eff}(-\boldsymbol{k})]^t$. Besides, for nonbianisotropic inclusions, such that $\underline{\boldsymbol{\alpha}}_{me}^{n} = \underline{\boldsymbol{\alpha}}_{em}^{n} = \underline{\boldsymbol{0}}$, $n = 1,2$, the bianistropy of the material only stems from the asymmetry introduced by phase propagation across the unit cell and in this case from the corresponding simplified form of (23), for centrosymmetric crystals it can be found that $\underline{\boldsymbol{\zeta}}_{\rm eff}(\boldsymbol{k}) = [\underline{\boldsymbol{\xi}}_{\rm eff}(\boldsymbol{k})]^t$. The latter property, in combination with reciprocity, implies that $\underline{\boldsymbol{\xi}}_{\rm eff}(\boldsymbol{k}) = -\underline{\boldsymbol{\xi}}_{\rm eff}(-\boldsymbol{k})$ and $\underline{\boldsymbol{\zeta}}_{\rm eff}(\boldsymbol{k}) = -\underline{\boldsymbol{\zeta}}_{\rm eff}(-\boldsymbol{k})$ [23].

IV. LONG WAVELENGTH LIMIT

In the long wavelength limit and far from the inclusion resonances, i.e., under the conditions $k_h a_i \ll 1$, $ka_i \ll 1$, $i = 1,2,3$, $\underline{\boldsymbol{C}}_{e,m} \sim 0$ and the bianistropic effects of the lattice are negligible and the coupling dyad becomes diagonal $\underline{\boldsymbol{C}}_{\rm int} \sim C_{\rm int}\underline{\boldsymbol{I}}$. Considering for simplicity the case of isotropic particles ($\underline{\boldsymbol{\alpha}}_{ee}^{n} = \alpha_{ee}^{n}\underline{\boldsymbol{I}}$, $\underline{\boldsymbol{\alpha}}_{mm}^{n} = \alpha_{mm}^{n}\underline{\boldsymbol{I}}$, $\underline{\boldsymbol{\alpha}}_{me}^{n} = \underline{\boldsymbol{\alpha}}_{em}^{n} = \underline{\boldsymbol{0}}$), the constitutive parameters become

$$\begin{aligned} \varepsilon_{\rm eff} &= \varepsilon_h \left\{1 + \frac{1}{V_{\rm cell}} \frac{\alpha_{ee}^1 + \alpha_{ee}^2 - 2\alpha_{ee}^1\alpha_{ee}^2[C_{\rm int}(0) - C_{\rm int}(\boldsymbol{r}_1 - \boldsymbol{r}_2)]}{1 - C_{\rm int}(0)\left(\alpha_{ee}^1 + \alpha_{ee}^2\right) + \alpha_{ee}^1\alpha_{ee}^2\{[C_{\rm int}(0)]^2 - [C_{\rm int}(\boldsymbol{r}_1 - \boldsymbol{r}_2)]^2\}}\right\}, \\ \mu_{\rm eff} &= \mu_h \left\{1 + \frac{1}{V_{\rm cell}} \frac{\alpha_{mm}^1 + \alpha_{mm}^2 - 2\alpha_{mm}^1\alpha_{mm}^2[C_{\rm int}(0) - C_{\rm int}(\boldsymbol{r}_1 - \boldsymbol{r}_2)]}{1 - C_{\rm int}(0)\left(\alpha_{mm}^1 + \alpha_{mm}^2\right) + \alpha_{mm}^1\alpha_{mm}^2\{[C_{\rm int}(0)]^2 - [C_{\rm int}(\boldsymbol{r}_1 - \boldsymbol{r}_2)]^2\}}\right\}. \end{aligned} \tag{24}$$

It is recognized that the above expressions reduce to the generalized Clausius-Mossotti relations for the effective permittivity and permeability of binary lattices in the static case [12,16]

$$\begin{aligned} \varepsilon_{\rm eff} &= \varepsilon_h \left[1 + \frac{1}{V_{\rm cell}} \frac{\left(\alpha_{ee}^1 + \alpha_{ee}^2\right)}{1 - \frac{1}{3V_{\rm cell}}\left(\alpha_{ee}^1 + \alpha_{ee}^2\right)}\right] \mu_{\rm eff} \\ &= \mu_h \left[1 + \frac{1}{V_{\rm cell}} \frac{\left(\alpha_{mm}^1 + \alpha_{mm}^2\right)}{1 - \frac{1}{3V_{\rm cell}}\left(\alpha_{mm}^1 + \alpha_{mm}^2\right)}\right], \end{aligned} \tag{25}$$

provided that we make use of the well-known relation

$$\underline{\boldsymbol{C}}_{\rm int}(\omega \to 0, \boldsymbol{k} \to 0) \sim \frac{1}{3V_{\rm cell}}\underline{\boldsymbol{I}}, \tag{26}$$

and we take into account that at $\omega = 0$ $C_{\rm int}(0) \sim C_{\rm int}(\boldsymbol{r}_1 - \boldsymbol{r}_2)$. However, neglecting the $(\omega,\boldsymbol{k})$ dependence of the interaction dyadics and actual particle displacement can give results significantly different from those obtained with the formulas developed in this work.

V. DISPERSION EQUATION AND EIGENMODAL PROPAGATION

The eigenmodal solutions corresponding to the waves that can propagate in the periodic array in the absence of external sources can be found by placing $\boldsymbol{E}_{\text{ext}} = \boldsymbol{H}_{\text{ext}} = 0$ in (14). Alternatively, to find the eigenmodes in the binary metamaterial we can exploit Maxwell's equations in the absence of sources

$$\boldsymbol{k} \times \boldsymbol{E}_{\text{av}} = \omega \boldsymbol{B}_{\text{av}}, \quad \boldsymbol{k} \times \boldsymbol{H}_{\text{av}} = -\omega \boldsymbol{D}_{\text{av}}. \tag{27}$$

Upon substitution of the constitutive relations (22), (27) can be rearranged as follows:

$$\begin{aligned} \underline{\boldsymbol{\mu}}_{\text{eff}}^{-1}\left(\frac{\boldsymbol{k}}{\omega} \times \boldsymbol{E}_{\text{av}} - \underline{\boldsymbol{\zeta}}_{\text{eff}} \cdot \boldsymbol{E}_{\text{av}}\right) &= \boldsymbol{H}_{\text{av}}, \\ \left(\frac{\boldsymbol{k}}{\omega} \times \underline{\boldsymbol{1}} + \underline{\boldsymbol{\xi}}_{\text{eff}}\right) \cdot \boldsymbol{H}_{\text{av}} &= -\underline{\boldsymbol{\varepsilon}}_{\text{eff}} \cdot \boldsymbol{E}_{\text{av}}. \end{aligned} \tag{28}$$

Combining the two expressions in (28) we obtain the following dispersion equation for a generic bianisotropic medium:

$$\left[\left(\frac{\boldsymbol{k}}{\omega} \times \underline{\boldsymbol{1}} + \underline{\boldsymbol{\xi}}_{\text{eff}}\right)\underline{\boldsymbol{\mu}}_{\text{eff}}^{-1}\left(\frac{\boldsymbol{k}}{\omega} \times \underline{\boldsymbol{1}} - \underline{\boldsymbol{\zeta}}_{\text{eff}}\right) + \underline{\boldsymbol{\varepsilon}}_{\text{eff}}\right] \cdot \boldsymbol{E}_{\text{av}} = 0. \tag{29}$$

The nontrivial solutions of this equation, obtained by equating to zero the determinant of the dyadic tensor multiplying $\boldsymbol{E}_{\text{av}}$, correspond to the specific pair $(\omega,\boldsymbol{k})$ satisfying the array dispersion relation and characterizing the eigenmodes propagating in the binary metamaterial. It is noted that solutions of (29) comprise both transverse and longitudinal eigenmodes.

VI. EQUIVALENT PARAMETERS

Standard homogenization procedures usually retrieve only two equivalent parameters, $\underline{\boldsymbol{\varepsilon}}_{\text{eq}}$ and $\underline{\boldsymbol{\mu}}_{\text{eq}}$, to macroscopically describe metamaterials by a local anisotropic constitutive model. As explained in [6,20], and also pointed out in the previous sections, these equivalent parameters embed the magnetoelectric coupling effects as a form of weak spatial dispersion. As a result, at frequencies where magnetoelectric coupling is non-negligible, equivalent parameters may exhibit nonphysical behavior, unlike the well-behaved *effective* parameters. This can be easily recognized by examining the relation between the effective parameters derived before and the equivalent ones. By using Maxwell's equations in the absence of sources and the constitutive relations (22) we can write

$$\begin{aligned} \boldsymbol{E}_{\text{av}} &= -\underline{\boldsymbol{\varepsilon}}_{\text{eff}}^{-1}\left(\frac{\boldsymbol{k}}{\omega} \times \underline{\boldsymbol{1}} + \underline{\boldsymbol{\xi}}_{\text{eff}}\right) \cdot \boldsymbol{H}_{\text{av}}, \\ \boldsymbol{H}_{\text{av}} &= \underline{\boldsymbol{\mu}}_{\text{eff}}^{-1}\left(\frac{\boldsymbol{k}}{\omega} \times \underline{\boldsymbol{1}} - \underline{\boldsymbol{\zeta}}_{\text{eff}}\right) \cdot \boldsymbol{E}_{\text{av}}. \end{aligned} \tag{30}$$

Substituting (30) into (22) we have

$$\begin{aligned} \boldsymbol{D}_{\text{av}} &= \left[\underline{\boldsymbol{\varepsilon}}_{\text{eff}} + \underline{\boldsymbol{\xi}}_{\text{eff}}\underline{\boldsymbol{\mu}}_{\text{eff}}^{-1}\left(\frac{\boldsymbol{k}}{\omega} \times \underline{\boldsymbol{1}} - \underline{\boldsymbol{\zeta}}_{\text{eff}}\right)\right] \cdot \boldsymbol{E}_{\text{av}} = \underline{\boldsymbol{\varepsilon}}_{\text{eq}} \cdot \boldsymbol{E}_{\text{av}}, \\ \boldsymbol{B}_{\text{av}} &= \left[\underline{\boldsymbol{\mu}}_{\text{eff}} - \underline{\boldsymbol{\zeta}}_{\text{eff}}\underline{\boldsymbol{\varepsilon}}_{\text{eff}}^{-1}\left(\frac{\boldsymbol{k}}{\omega} \times \underline{\boldsymbol{1}} + \underline{\boldsymbol{\xi}}_{\text{eff}}\right)\right] \cdot \boldsymbol{H}_{\text{av}} = \underline{\boldsymbol{\mu}}_{\text{eq}} \cdot \boldsymbol{H}_{\text{av}}. \end{aligned} \tag{31}$$

Comparing (31) to the constitutive relations for an anisotropic material the equivalent parameters can be expressed as

$$\begin{aligned} \underline{\boldsymbol{\varepsilon}}_{\text{eq}} &= \underline{\boldsymbol{\varepsilon}}_{\text{eff}} + \underline{\boldsymbol{\xi}}_{\text{eff}}\underline{\boldsymbol{\mu}}_{\text{eff}}^{-1}\left(\frac{\boldsymbol{k}}{\omega} \times \underline{\boldsymbol{1}} - \underline{\boldsymbol{\zeta}}_{\text{eff}}\right), \\ \underline{\boldsymbol{\mu}}_{\text{eq}} &= \underline{\boldsymbol{\mu}}_{\text{eff}} - \underline{\boldsymbol{\zeta}}_{\text{eff}}\underline{\boldsymbol{\varepsilon}}_{\text{eff}}^{-1}\left(\frac{\boldsymbol{k}}{\omega} \times \underline{\boldsymbol{1}} + \underline{\boldsymbol{\xi}}_{\text{eff}}\right). \end{aligned} \tag{32}$$

As evident, both the equivalent permittivity and equivalent permeability also include the magnetoelectric coupling effects and contain an explicit dependence on $\boldsymbol{k}$. It can be shown that the relations derived coincide with those developed in [6,20]. Since derivation of (32) relies on the use of Maxwell equation in the absence of impressed sources it is implicit that the description with the equivalent parameters is valid only for eigenmodal propagation.

VII. POWER AND MACROSCOPIC POYNTING VECTOR

To gain further insight into the metamaterial electromagnetic response, it is useful to make some considerations about power. The spatially averaged macroscopic Poynting vector is defined as the average over the cell of the microscopic Poynting vector, i.e.,

$$\boldsymbol{S}_{\text{av}} = \frac{1}{V_{\text{cell}}} \iiint_{\Omega} \frac{1}{2}\text{Re}\{\boldsymbol{E}(\boldsymbol{r}) \times \boldsymbol{H}^{*}(\boldsymbol{r})\} d^{3}\boldsymbol{r}. \tag{33}$$

The expansion of the microscopic fields in terms of Floquet space harmonics

$$\begin{aligned} \boldsymbol{E}(\boldsymbol{r}) &= \sum_{\boldsymbol{I}} \boldsymbol{E}_{\boldsymbol{I}} e^{i\boldsymbol{k}\cdot\boldsymbol{r}} e^{i\boldsymbol{k}_{\boldsymbol{I}}\cdot\boldsymbol{r}} \\ &= \boldsymbol{E}_{\text{av}} e^{i\boldsymbol{k}\cdot\boldsymbol{r}} + e^{i\boldsymbol{k}\cdot\boldsymbol{r}} \sum_{\boldsymbol{I}\neq(0,0,0)} \boldsymbol{E}_{\boldsymbol{I}} e^{i\boldsymbol{k}_{\boldsymbol{I}}\cdot\boldsymbol{r}}, \\ \boldsymbol{H}(\boldsymbol{r}) &= \sum_{\boldsymbol{I}} \boldsymbol{H}_{\boldsymbol{I}} e^{i\boldsymbol{k}\cdot\boldsymbol{r}} e^{i\boldsymbol{k}_{\boldsymbol{I}}\cdot\boldsymbol{r}} \\ &= \boldsymbol{H}_{\text{av}} e^{i\boldsymbol{k}\cdot\boldsymbol{r}} + e^{i\boldsymbol{k}\cdot\boldsymbol{r}} \sum_{\boldsymbol{I}\neq(0,0,0)} \boldsymbol{H}_{\boldsymbol{I}} e^{i\boldsymbol{k}_{\boldsymbol{I}}\cdot\boldsymbol{r}} \end{aligned} \tag{34}$$

is interpreted as the superposition of the $\boldsymbol{I} = (0,0,0)$ harmonic, corresponding to the homogenized average electric $\boldsymbol{E}_{\text{av}}$ and magnetic $\boldsymbol{H}_{\text{av}}$ fields, and all the higher order harmonics $\boldsymbol{I} \neq (0,0,0)$ providing the fluctuation of the microscopic fields around their averages. By exploiting (34) and Floquet harmonic power orthogonality, the spatially averaged Poynting vector (33) can be split into the sum of two terms associated to the macroscopic fields and to the fluctuation of the microscopic fields, respectively,

$$\boldsymbol{S}_{\text{av}} = \frac{1}{2}\text{Re}\left\{\boldsymbol{E}_{\text{av}} \times \boldsymbol{H}_{\text{av}}^{*}\right\} + \sum_{\boldsymbol{I}\neq(0,0,0)} \frac{1}{2}\text{Re}\{\boldsymbol{E}_{\boldsymbol{I}} \times \boldsymbol{H}_{\boldsymbol{I}}^{*}\}. \tag{35}$$

Indeed because of the nonlinear nature of power definition, the zero-average fluctuation of the microscopic fields also contributes to the average macroscopic Poynting vector [24].

On the other hand, according to the proposed homogenized model for the bulk material, described by its effective constitutive parameters, the Poynting vector can be expressed as that in a homogeneous material. As highlighted in [2,25],

spatial dispersion has to be duly taken into account to exactly determine the energy flux density. In a transparent (i.e., lossless) medium the spatial dispersion is in fact responsible for the appearance of an additional term in the definition of the Poynting vector. The formula provided in [2,25] for a spatially dispersive medium characterized only by the permittivity, can be easily extended to a composite structure described by a homogenized bianisotropic model

$$\boldsymbol{S}^h_{\rm av} = \boldsymbol{S}_0 + \boldsymbol{S}_1 = \frac{1}{2}{\rm Re}\{\boldsymbol{E}_{\rm av} \times \boldsymbol{H}^*_{\rm av}\} - \frac{1}{4}\omega\nabla_{\boldsymbol{k}}[\boldsymbol{E}^*_{\rm av} \cdot \underline{\boldsymbol{\varepsilon}}_{\rm eff}(\omega,\boldsymbol{k}) \cdot \boldsymbol{E}_{\rm av} + \boldsymbol{E}^*_{\rm av} \cdot \underline{\boldsymbol{\xi}}_{\rm eff}(\omega,\boldsymbol{k}) \cdot \boldsymbol{H}_{\rm av} + \boldsymbol{H}^*_{\rm av} \cdot \underline{\boldsymbol{\zeta}}_{\rm eff}(\omega,\boldsymbol{k}) \cdot \boldsymbol{E}_{\rm av} + \boldsymbol{H}^*_{\rm av} \cdot \underline{\boldsymbol{\mu}}_{\rm eff}(\omega,\boldsymbol{k}) \cdot \boldsymbol{H}_{\rm av}], \quad (36)$$

where $\nabla_k = \sum_{p=1}^{3} \frac{\partial}{\partial k_p}\hat{\boldsymbol{u}}_p$ is the nabla differential operator with respect to $\boldsymbol{k}$. By comparing (35) and (36) the coincidence of the first terms is evident; also the second terms are expected to substantially correspond as far as spatial dispersion is weak. Indeed, the importance of the additional term appearing in (36) involving partial derivatives of the constitutive parameters with respect to the wave number to correctly calculate the macroscopic Poynting vector within the framework of an effective medium theory for either natural media or arbitrary metamaterials has been discussed in a few previous works [24,26–28]. Results of numerical comparisons between $\boldsymbol{S}_{\rm av}$ and $\boldsymbol{S}^h_{\rm av}$ are presented in the following section dedicated to the homogenization of sample metamaterial structures.

VIII. NUMERICAL RESULTS AND DISCUSSION

The formulation developed in this paper is general and can be applied to lossy, bianisotropic and magnetodielectric inclusions, and arbitrary source distribution. However, numerical results presented in this section are obtained by the application of the proposed GLL formulas for the effective parameters of binary metamaterials limitedly to the case of superlattices whose unit cell consists of two different types of lossless dielectric inclusions and eigenmodal propagation. In particular, we consider certain metamaterial configurations that have been proposed or examined in the previous literature with the twofold aim of validating these GLL formulas and showing the difference between this homogenization theory and techniques based on the extraction of effective material parameters from eigenmodal solutions. In all the following examples, metamaterial inclusions are spherical and their electric and magnetic polarizabilities are obtained from the exact Mie solution for the scattering from an isolated sphere [29]. It is noteworthy that for close packed arrays more accurate estimations of the polarizabilities, including the additional capacitive effects from neighboring spheres, could be obtained by the method outlined in [30].

As the first example, we examine the properties of the binary metamaterial structure proposed in [10,11] and then further analyzed in [12,17], that consists of a fcc arrangement of spherical inclusions of the same dielectric material but of different sizes, as depicted in Fig. 1. The superposition of the Mie electric and magnetic resonances of these two sets of spheres can excite both electric and magnetic dipole resonance modes in the structure, and lead to the creation of

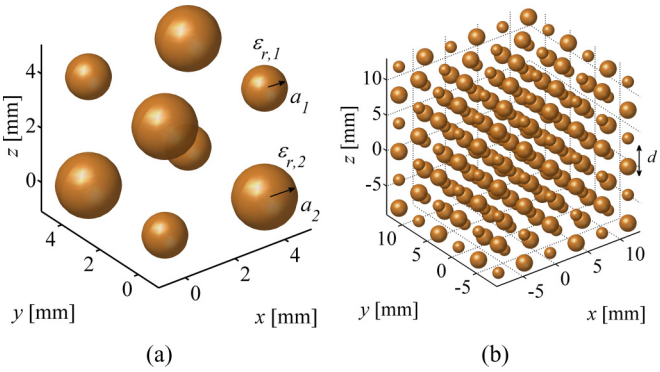

FIG. 1. (Color online) Geometry of a binary metamaterial crystal with a fcc lattice comprising two dielectric inclusions of the same dielectric material with $\varepsilon_{r,1} = \varepsilon_{r,2} = 400$ but with different radii $a_1 = 0.748$ mm and $a_2 = 1.069$ mm [10–12,17]. (a) The unit cell and (b) an illustrative portion of the metamaterial lattice.

a 3D isotropic medium with simultaneous negative effective permittivity and permeability. We refer in particular to the results presented in Figs. 2–4 of [17] for the dispersion diagram and the effective parameters of a binary metamaterial of lossless dielectric spheres characterized by the same relative permittivity $\varepsilon_{r,1} = \varepsilon_{r,2} = 400$, and with radii $a_1 = 0.748$ mm and $a_2 = 1.069$ mm. The period of the lattice is $d = 4$ mm. The propagation vector is assumed along the z direction, namely $\boldsymbol{k} = k\hat{\boldsymbol{z}}$, and the host medium is free space. The dispersion diagram for the transverse mode calculated by (29) is plotted in Fig. 2 and compared with the corresponding results obtained by Shore and Yaghjian (SY) (cf. Fig. 2 in [17]) and with full wave (FW) simulations. As apparent, the dispersion curves calculated by the GLL approach are in perfect agreement with those determined in [17] through a spherical modal analysis. The agreement is very good also with the FW analysis performed with Ansys HFSS, except for the presence of the additional mode plotted in green dots that is practically superimposed with the backward wave branch existing for $0.825 \leqslant (\omega/c)d \leqslant 0.85$. The FW simulation of

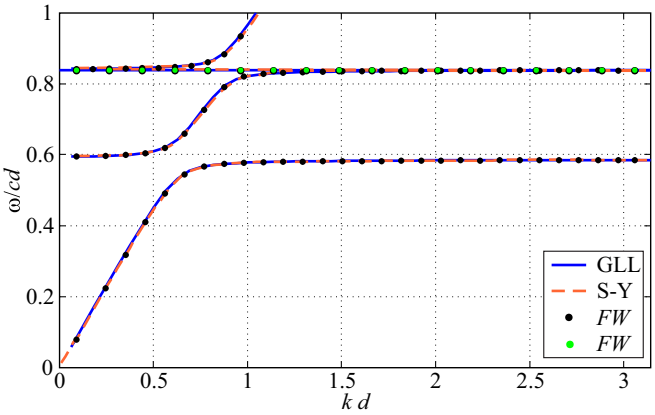

FIG. 2. (Color online) Dispersion diagram for the binary fcc lattice of dielectric spheres from Fig. 1. Curves calculated by the extended GLL method (solid blue lines) are compared with the plots provided in Fig. 2 of [17] (dashed red lines) and results of FW simulations performed with Ansys HFSS (black and green dots, for dipolar and multipolar resonance modes, respectively).

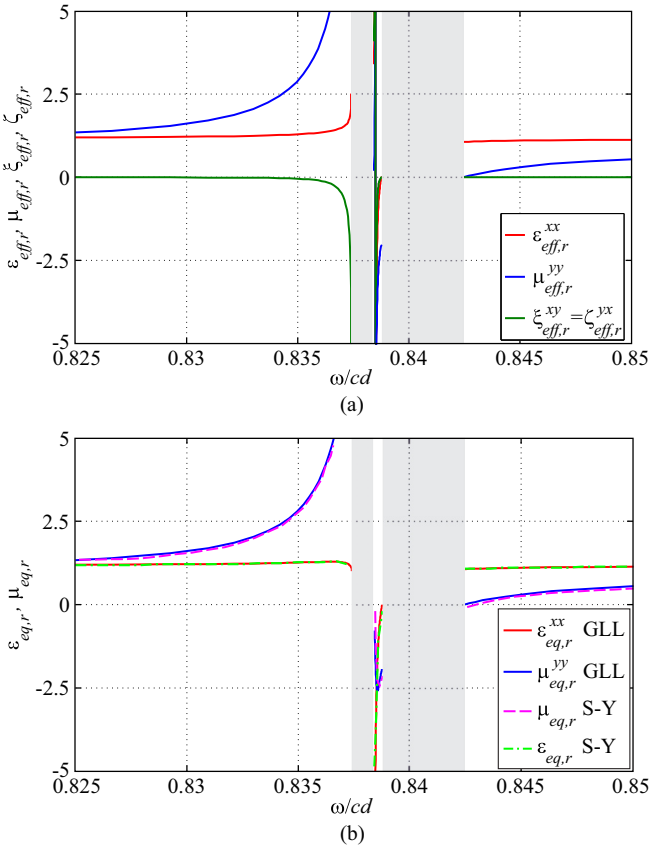

FIG. 3. (Color online) (a) Effective and (b) equivalent relative permittivity and permeability for the binary fcc lattice of dielectric spheres from Fig. 1. GLL method results for the equivalent parameters are compared with those from Shore and Yaghjian (SY) [17] (gray shaded regions denote band gaps).

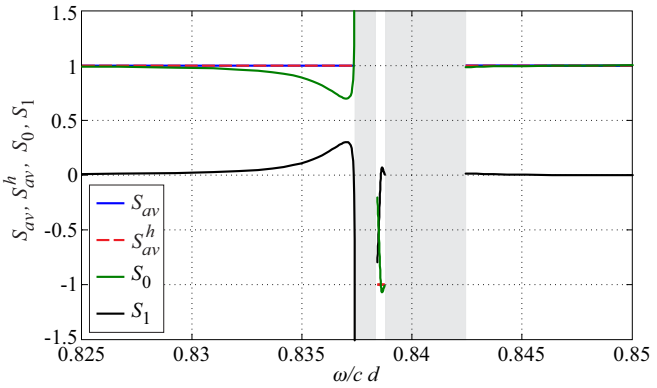

FIG. 4. (Color online) Average macroscopic Poynting vector for the transverse mode (normalized to unit power density) calculated in terms of Floquet space harmonics ($\boldsymbol{S}_{\rm av}$), or by formula (36) for the Poynting vector of a homogenized spatial dispersive medium ($\boldsymbol{S}^{h}_{\rm av}$), compared with the contributions of the macroscopic fields to the average Poynting vector ($\boldsymbol{S}_0$) and that related to spatial dispersion effects ($\boldsymbol{S}_1$) for the binary lattice from Fig. 1 (gray shaded regions denote band gaps).

the corresponding field pattern has revealed that the mode is supported by a higher order multipole resonance of the spherical inclusions. It is therefore not surprising that this mode is not discovered by the proposed GLL method due to the underlying dual dipole approximation for the current distribution induced in the inclusions, which implies that the method cannot predict propagating modes associated with high order multipole distribution of the field in the constituent particles.

In Fig. 3(a) is plotted the frequency dispersion of the effective parameters calculated by means of (23) for the specific pairs $(\omega,\boldsymbol{k})$ corresponding to the high frequency portion of the dispersion diagram in Fig. 2 centered around the backward wave branch $0.825 \leqslant (\omega/c)d \leqslant 0.85$. Moreover, in Fig. 3(b) the equivalent parameters calculated through the GLL method and (32) are compared with the equivalent permittivity $\underline{\boldsymbol{\varepsilon}}_{\rm eq}$ and permeability $\underline{\boldsymbol{\mu}}_{\rm eq}$ obtained in [17] from the eigenmodal analysis and by writing the constitutive relations as in a local isotropic material [6]. As apparent, the effective parameters derived in [17] practically coincide with the equivalent parameters $\underline{\boldsymbol{\varepsilon}}_{\rm eq}$, $\underline{\boldsymbol{\mu}}_{\rm eq}$ obtained by the GLL approach. However, as highlighted in [6], the equivalent parameters inherently contain a hidden form of weak spatial dispersion associated with magnetoelectric coupling, and this may translate into inconsistencies and lack of physical meaning in their dispersion. This can be easily discerned by comparing Figs. 3(a) and 3(b). It can be observed that in the low-frequency regime, well below the first band gap, equivalent and effective parameters coincide: they are both positive and practically constant with frequency. In this limit, classic homogenization techniques apply very well, and the metamaterial behaves as a regular mixture. Approaching the band gap, the *effective* permittivity maintains its physical meaning and exhibits a typical Lorentzian dispersion and positive slope. On the contrary, the equivalent permittivity experiences an anomalous antiresonant response. This is a typical behavior of the permittivity obtained by standard retrieval techniques, due to the fact that it includes the effect of magnetoelectric coupling, i.e., the contribution of the average magnetic field to the average electric polarization.

In Fig. 4 is plotted the average macroscopic Poynting vector, calculated by using both expressions (35) and (36), for the above investigated transverse mode, whose amplitude is normalized to have unit power density $|\boldsymbol{S}_{\rm av}| = 1$ at any frequency. Not unexpectedly, these two curves practically coincide, and their sign, which represents the direction of the group velocity and total energy of the propagating modal wave with respect to the phase velocity, i.e., the wave vector, which is assumed to be oriented along the positive z axis, is consistent with the slope of the various branches of the dispersion diagram in Fig. 2, as well as with the sign of the equivalent parameters. It can also be observed that the macroscopic field provides the dominant contribution $\boldsymbol{S}_0$ to the average Poynting vector, whereas the additional term $\boldsymbol{S}_1$ appearing in (36), which is related to spatial dispersion effects, is practically negligible everywhere except for the region where the mode is backward and close to the preceding band gap. By the low frequency edge of such band gap, $\boldsymbol{S}_1$ flows in the opposite direction with respect to $\boldsymbol{S}_0$ and the direction of propagation, and its amplitude progressively increases to determine the vanishing of the total power flow in the band gap. Instead, in the backward region $\boldsymbol{S}_1$ is predominantly parallel to $\boldsymbol{S}_0$ and counterdirected the wave vector, with the exclusion

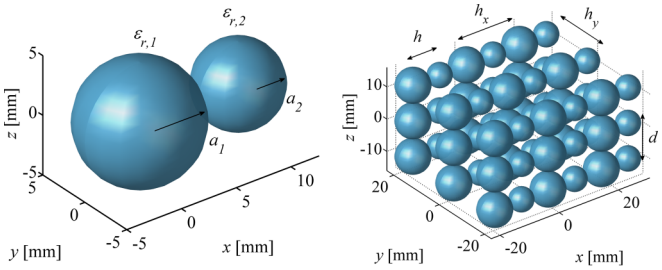

FIG. 5. (Color online) Geometry of a binary lattice metamaterial composed of two sets of dielectric spheres of the same dielectric material $\varepsilon_{r,1} = \varepsilon_{r,2} = 40$ but of different size $a_1 = 0.5$ and $a_2 = 0.356$ cm [18]. (a) The unit cell and (b) an illustrative portion of the metamaterial lattice.

of a small range near the high-frequency mode-gap edge. It is further noted that $\boldsymbol{S}_0$ making the prevailing contribution to $\boldsymbol{S}_{\rm av}$ and being parallel to it over all the examined frequency range ensures the accordance between the trend of equivalent parameters and the dispersion curves.

To illustrate that the developed GLL method is applicable to arbitrary binary lattice configurations, in contrast to homogenization techniques previously reported which are restricted to specific binary lattice geometries and/or propagation directions [17,18], we have further analyzed the metamaterial structure characterized in Fig. 7 of [18] by using the same spherical modal analysis originally proposed in [19]. As in the previous example, this structure is formed by a periodical arrangement of dielectric spheres with the same relative permittivity but two different sizes. However, the array is no longer a fcc lattice but is instead organized into alternating planes of same particles which are orthogonal to the array axis, as shown in Fig. 5. In particular, the inclusions have relative permittivity $\varepsilon_{r,1} = \varepsilon_{r,2} = 40$ and radii equal to $a_1 = 0.5$ and $a_2 = 0.356$ cm. The periods of the cell are $h_x = h_y = 1.8$ cm, $d = 1.1$ cm along the x,y,z directions, respectively, and the distance between the planes containing spheres of the different size is $h = h_x/2$. The background is free space and the propagation vector $\boldsymbol{k} = k\hat{\boldsymbol{z}}$ is assumed along the z axis.

The dispersion diagram for the x-polarized transverse modes propagating in this composite as calculated by (29) is plotted in Fig. 6 in comparison with the corresponding results obtained by Ghadarghadr and Mosallaei (GM) in Fig. 7 of [18]. GLL results have been further validated by performing also FW calculations of the dispersion diagram of this structure with CST Microwave Studio. While between GLL and GM dispersion curves there is some disagreement at higher frequencies, generally the GLL dispersion data agree well with FW results, except for the existence of the additional mode between $1.5 \leqslant kd \leqslant 1.58$ revealed by FW simulations and not detected by the GLL analysis. However, also for this structure, inspection of the FW simulated pattern of the mode field distribution has revealed that the mode is associated with a higher order multipole resonance of the inclusions, which cannot be discovered with the dual dipole approximation used in the GLL technique.

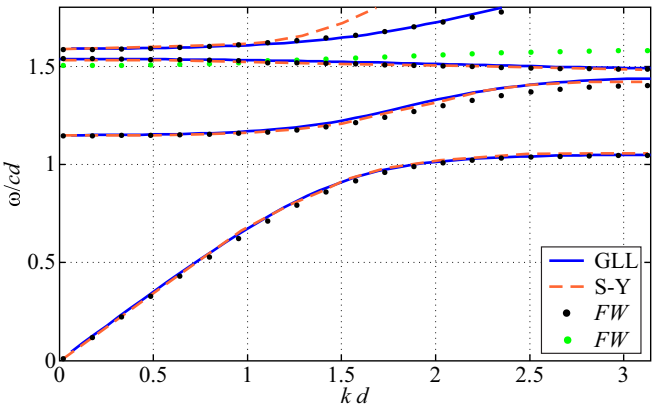

FIG. 6. (Color online) Dispersion diagram for the binary lattice depicted in Fig. 5. Curves calculated by the extended GLL method (solid blue lines) are compared with corresponding results in Fig. 7 of [18] (GM, dashed red lines) and results of FW simulations with CST Microwave Studio (black and green dots, for dipolar and multipolar resonance modes, respectively).

The effective and equivalent parameters corresponding to the eigenmodal solutions are plotted in Figs. 7(a) and 7(b), respectively. As in the previous example, near the band gap regions the equivalent parameters exhibit antiresonant and nonphysical artifacts, which are a symptom of non-negligible

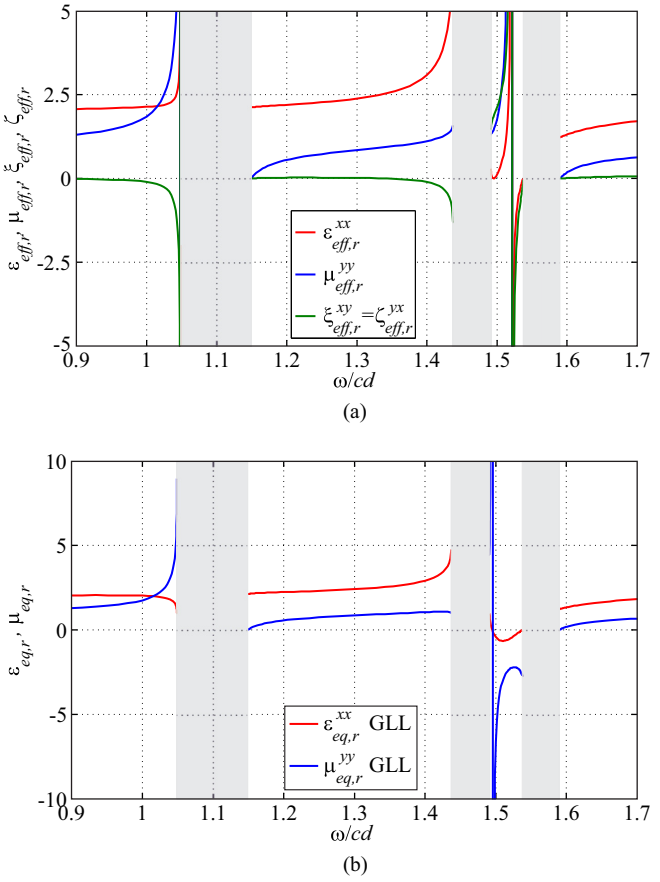

FIG. 7. (Color online) (a) Effective and (b) equivalent relative parameters for the binary lattice depicted in Fig. 5 (gray shaded regions denote band gaps).

spatial dispersion and magnetoelectric coupling in the array, which is not unexpected in such a dense structure. Indeed, correctly taking into account the magnetoelectric coupling hidden in the equivalent parameters through the improved bianisotropic constitutive model (23) and the introduction of $\underline{\boldsymbol{\xi}}_{\text{eff}}, \underline{\boldsymbol{\zeta}}_{\text{eff}}$ results in a causal Lorentzian response for both the effective permittivity and permeability near the low frequency resonance of the inclusions, accompanied by an analogous non-negligible resonance of $\underline{\boldsymbol{\xi}}_{\text{eff}}(\underline{\boldsymbol{\zeta}}_{\text{eff}})$. The significant divergence between equivalent and effective parameters for frequencies below the first band gap evident from Figs. 7(a) and 7(b) proves the relevance of magnetoelectric effects that cannot be neglected even in the long-wavelength regime. However, the introduction of $\underline{\boldsymbol{\xi}}_{\text{eff}}, \underline{\boldsymbol{\zeta}}_{\text{eff}}$ in the metamaterial model does not seem to completely restore the local nature of the permittivity and permeability for the considered structure: at frequencies corresponding to the backward wave branch of the dispersion diagram at $1.491 \leqslant kd \leqslant 1.538$, above the second band gap, the effective permittivity still exhibits an apparently nonphysical negative slope. However, it must be noticed that the effective parameters are here calculated along the dispersion curves, i.e., as $\underline{\boldsymbol{\varepsilon}}_{\text{eff}}(\omega, \boldsymbol{k}(\omega))$, $\underline{\boldsymbol{\mu}}_{\text{eff}}(\omega, \boldsymbol{k}(\omega))$, and not for a fixed wave number $\boldsymbol{k}$ and varying ω, which is the condition for the validity of Kramers-Kronig relations in the case of spatially dispersive materials [2,25,26]. Indeed, we have repeated the calculations of the effective parameters for variable ω at several fixed values of $\boldsymbol{k}$ without observing any unphysical negative slope behavior. Such plots are not reported here due to space limitation.

Moreover, in the range of frequencies corresponding to the backward mode of the dispersion diagram, one would expect to have both negative equivalent permittivity and permeability, whereas by inspection of Fig. 7(b) it can be seen that this is not the case.

To clarify this issue, it is useful to consider the power flow into this metamaterial that can be calculated by either using (35), which expresses the average macroscopic Poynting vector in terms of Floquet space harmonics, or formula (36) for the Poynting vector of a homogenized spatially dispersive medium. These quantities are compared in Fig. 8, where for simplicity the mode amplitude is normalized to have unit power density $|\boldsymbol{S}_{\text{av}}| = 1$. In Fig. 8 are also plotted the contribution $\boldsymbol{S}_0$ of the macroscopic fields to the average Poynting vector, and the additional term $\boldsymbol{S}_1$ appearing in (36) related to spatial dispersion effects. As apparent, $\boldsymbol{S}_{\text{av}}$ and $\boldsymbol{S}^h_{\text{av}}$ are superimposed over most of the eigenmode dispersion range, and a small disagreement is observed only at the lower edge of the first band gap, likely because of stronger spatial dispersion effects; moreover, the sign of $\boldsymbol{S}_{\text{av}}$ and $\boldsymbol{S}^h_{\text{av}}$ gives both the direction of the group velocity and total energy of the propagating wave with respect to the phase velocity, i.e., the wave vector, which is fixed along the positive z direction. Comparing Fig. 8 with the dispersion diagram for the x-polarized transverse mode plotted in Fig. 6, it can be observed that when the eigenmode solution is forward, i.e., when the slope of the wave dispersion curves is positive, the sign of $\boldsymbol{S}_{\text{av}}$ (and of $\boldsymbol{S}^h_{\text{av}}$) is positive as well, which means that, as expected, phase and energy velocities are in the same direction. Instead, in the frequency region of the dispersion diagram for $1.491 \leqslant kd \leqslant 1.538$, the sign of $\boldsymbol{S}_{\text{av}}$ is negative, which clearly

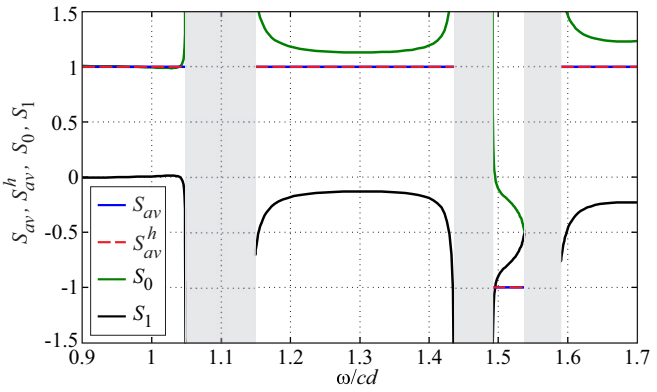

FIG. 8. (Color online) Average macroscopic Poynting vector for the x-polarized transverse mode (normalized to unit power density) calculated in terms of Floquet space harmonics ($\boldsymbol{S}_{\text{av}}$), or by formula (36) for the Poynting vector of a homogenized spatial dispersive medium ($\boldsymbol{S}^h_{\text{av}}$), compared with the contributions of the macroscopic fields to the average Poynting vector ($\boldsymbol{S}_0$) and that related to spatial dispersion effects ($\boldsymbol{S}_1$) for the binary lattice from Fig. 5 (gray shaded regions denote band gaps).

indicates an effective negative index dispersion mode (backward wave) having counterpropagating phase and energy. It is also interesting to examine the relative magnitude of $\boldsymbol{S}_0$ and $\boldsymbol{S}_1$ and their respective contribution to $\boldsymbol{S}^h_{\text{av}}$. From inspection of (35) and (36), it appears that $\boldsymbol{S}_1$ takes into account both the impact of spatial dispersion effects and the contribution of spatial harmonics of higher order to the average Poynting vector. In most of the frequency range the fundamental space harmonic appears to provide a satisfactory approximation of the actual Poynting vector and is the dominant contribution from an energetic point of view. However, spatial harmonics of higher order also carry a relevant portion of power at certain frequencies near the edges of the band gaps, where we can see that $\boldsymbol{S}_1$ flows in the opposite direction with respect to the Poynting vector of the fundamental harmonic $\boldsymbol{S}_0$. In particular, near the (low-frequency) band-gap-backward mode edge, $\boldsymbol{S}_1$ becomes the dominant contribution to the total power flux. At these frequencies, while $\boldsymbol{S}_0$ flows in the direction of propagation, and indeed we have positive values of the equivalent parameters, $\boldsymbol{S}_1$ and the total power $\boldsymbol{S}^h_{\text{av}}$ flow in the opposite direction as a backward mode requires. This finally explains the non-negative value of the equivalent parameters associated to the fundamental harmonic for some $(\omega, \boldsymbol{k})$ pairs of the backward eigenmode solution. Thus we can conclude that when the contribution of $\boldsymbol{S}_1$ is non-negligible, spatial dispersion must be duly taken into account, for example in the calculation of the power flow associated with propagation across the metamaterial; at the same time, such spatial dispersion effects are inextricably connected with the onset of higher order harmonics, whose relevance in the description of the microscopic field might imply that homogenized parameters are inherently nonlocal, i.e., spatially dispersive. Indeed, only if one single space harmonic is dominating, and the microscopic field is thus well approximated by a single uniform plane wave, as in most natural materials, the periodic structure behaves as a local homogenized material with the permittivity and permeability of that space harmonic [31].

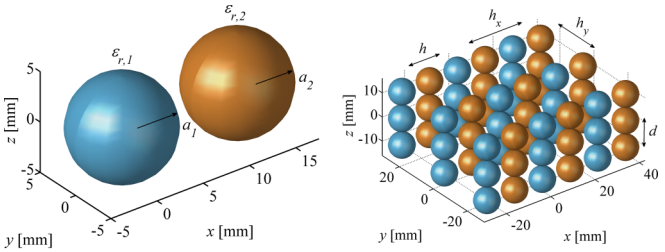

FIG. 9. (Color online) Geometry of a binary lattice metamaterial consisting of two sets of dielectric spheres of the same size $a_1 = a_2 = 0.5$ cm but of materials with different permittivities $\varepsilon_{r,1} = 40$ and $\varepsilon_{r,1} = 20.5$. (a) The unit cell and (b) an illustrative portion of the metamaterial lattice.

The last example we present is relevant to the analysis of another structure considered in [18], where the spherical inclusions have the same size but are made of different materials. The geometric arrangement of the particles is shown in Fig. 9. The permittivities of the two types of particles are $\varepsilon_{r,1} = 40$ and $\varepsilon_{r,2} = 20.5$. The periodicity of the unit cell along the x,y,z directions are $h_x = h_y = 2.5$ cm, $d = 1.1$ cm and the distance between the planes containing spheres of different permittivity is $h = h_x/2$. The radius of the particles is $a_1 = a_2 = 0.5$ cm.

Figures 10, 11(a), and 11(b) show the dispersion diagram for the x-polarized transverse mode, and the effective and equivalent parameters for the eigenmode solutions, respectively. In Fig. 10 the dispersion curves obtained by the GLL method are compared with corresponding results by Ghadarghadr-Mosallaei (GM) and FW simulation data. The GLL approach and FW analysis show a good agreement except for the additional mode at $1.494 \leqslant kd \leqslant 1.59$ associated with higher order multipole resonance of the inclusions that can be found only through the FW eigenmode simulation (green dots in Fig. 10). Similarly to the previous example, it can be observed that on the one hand the equivalent parameters

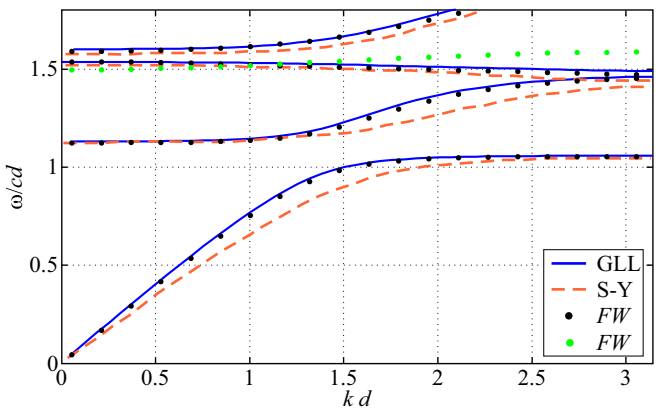

FIG. 10. (Color online) Dispersion diagram for the binary lattice depicted in Fig. 9. Curves calculated with the extended GLL method (solid blue lines) are compared with corresponding results in Fig. 4 of [18] (GM, dashed red lines), and FW simulations (black and green dots, for the dipolar and multipolar resonance modes, respectively).

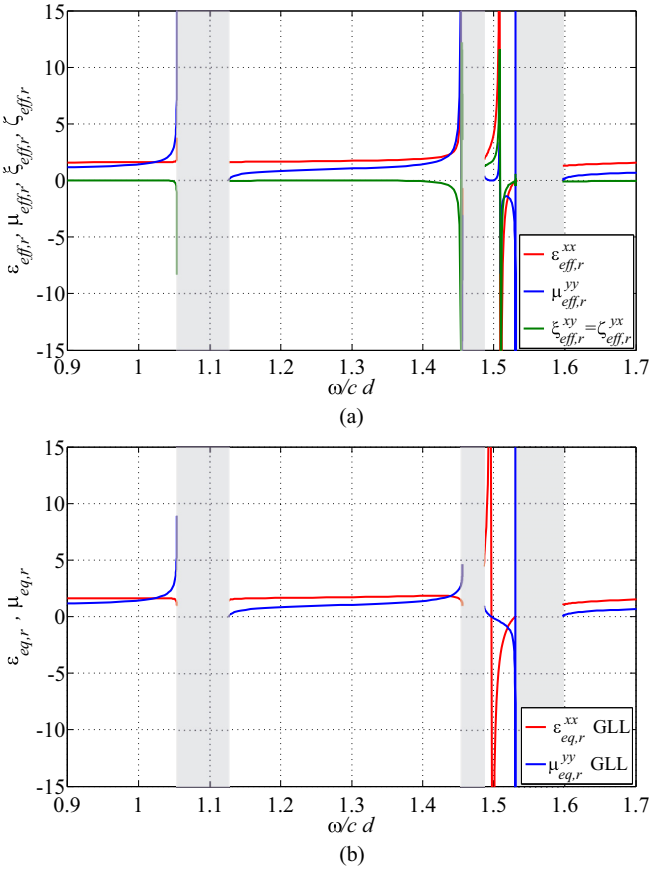

FIG. 11. (Color online) (a) Effective and (b) equivalent relative parameters for the binary lattice depicted in Fig. 9 (gray shaded regions denote band gaps).

contain a hidden form of weak spatial dispersion associated with magnetoelectric coupling which results in artifacts and nonphysical features in their behavior, and on other hand in the frequency range $1.486 \leqslant kd \leqslant 1.531$ corresponding to the backward wave branch of the dispersion diagram, the equivalent permittivity and permeability are not always simultaneously negative. At the same time the effective parameters in the backward wave frequency range still exhibits an apparently nonphysical negative slope, but, as explained with reference to the previous example of metamaterial structure [cf. Fig. 7(a)], this does not impair their physical meaningfulness because the wave vector is not fixed in the plots shown, as required for the validity of Kramers-Kronig relations in the case of spatially dispersive materials [2,25,26].

To explain the inconsistencies noted in the equivalent parameters, we have again calculated the Poynting vector according to both (35) and (36). $\boldsymbol{S}_{\rm av}$ and $\boldsymbol{S}^h_{\rm av}$, normalized to $|\boldsymbol{S}_{\rm av}| = 1$, are plotted against frequency in Fig. 12, together with the quantities $\boldsymbol{S}_0$ and $\boldsymbol{S}_1$. As in the previous examples, the spatially macroscopic Poynting vector $\boldsymbol{S}_{\rm av}$ and the Poynting vector of the homogenized medium $\boldsymbol{S}^h_{\rm av}$ coincide everywhere except that at the edges of the band gaps, because of the nonweak spatial dispersion at those frequencies; the sign of $\boldsymbol{S}_{\rm av}$ and $\boldsymbol{S}^h_{\rm av}$ is in agreement with the slope, i.e., the group velocity, of the branches of the dispersion diagram in Fig. 10. As

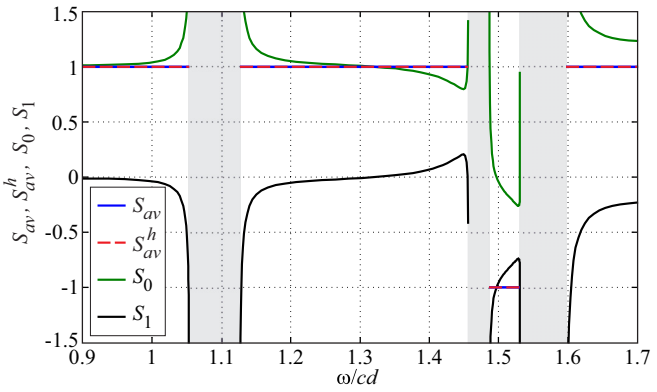

FIG. 12. (Color online) Average macroscopic Poynting vector of an x-polarized transverse mode (with normalized unit power density) calculated in terms of Floquet space harmonics ($\boldsymbol{S}_{\mathrm{av}}$), or by formula (36) for the Poynting vector of a homogenized spatial dispersive medium, compared with the contributions of the macroscopic fields to the average Poynting vector ($\boldsymbol{S}_0$) and that related to spatial dispersion effects ($\boldsymbol{S}_1$) for the metamaterial with binary lattice from Fig. 9 (gray shaded regions denote band gaps).

apparent by comparing $\boldsymbol{S}_0$, $\boldsymbol{S}_1$, and $\boldsymbol{S}^h_{\mathrm{av}}$, the fundamental space harmonic provides the dominant contribution to the total power in most of the examined frequency range, while near the band gaps a significant portion of the power is instead associated with higher order space harmonics which flows in the opposite direction with respect to the direction of propagation. At some frequencies in the range corresponding to the backward mode branch, the higher order space harmonics carry the dominant contribution of the power, which flows in the opposite direction with respect to the Poynting vector of the fundamental harmonic, thus restoring the accordance of the total power flow direction with the negative group velocity associated with the backward mode. This explains the unexpected positive values of the equivalent parameters for some eigenmodal solutions in the backward mode, being these parameters associated only with the fundamental space harmonic whose power flows is in the direction of propagation. Being $\boldsymbol{S}_1$ connected to spatial dispersion effects it can be underlined once more the necessity to duly take into account spatial dispersion to provide a correct description of the energy flux density in the homogenized material.

IX. CONCLUSION

We have developed generalized Lorentz-Lorenz formulas for the effective parameters of binary lattice metamaterials composed of a periodic arrangement of electric and/or magnetic inclusions. The derivation is accomplished within a Floquet-based approach and using a dual dipole approximation for the induced currents. The obtained formulas for the metamaterial effective electric and magnetic characteristics extend previous formulations valid for a dielectric and/or magnetic crystal comprising one particle per unit cell and duly consider both electric and magnetic polarizabilities and naturally describe the effects of frequency and spatial dispersion. Our formulas take into account the full dynamic coupling in dense periodic lattices and provide a physically sounded description of a wide class of binary metamaterials that remains valid also when the density of inclusions is not small and classic homogenization models, like Clausius-Mossotti relations, based on quasistatic assumptions and thus neglecting the phase variation across the unit cell of the periodic lattice, lose their accuracy.

Numerical example have been presented to show that the developed GLL method is applicable to arbitrary binary lattice configurations, in contrast to homogenization techniques previously proposed which are restricted to specific binary lattice geometries and/or propagation directions.

An investigation of the power associated with the fundamental and higher order Floquet space harmonics of the microscopic field has been performed to clarify certain inconsistencies appearing in the equivalent parameters. This analysis has demonstrated that spatial dispersion must be duly taken into account to correctly describe the power flow associated to propagation across the metamaterial, and that spatial dispersion effects are linked to the relevance of higher order Floquet harmonics in the description of the microscopic field, bringing as a consequence that when such harmonics are non-negligible, homogenized parameters are inherently nonlocal.

[1] G. W. Milton, *The Theory of Composites, Cambridge Monographs on Applied and Computational Mathematics* (Cambridge University Press, Cambridge, 2002).

[2] L. D. Landau and E. M. Lifshitz, *Electrodynamics of Continuous Media, Course of Theoretical Physics* (Elsevier, Butterworth-Heinemann, Amsterdam, 2004), Vol. 8.

[3] M. G. Silveirinha, Metamaterial homogenization approach with application to the characterization of microstructured composites with negative parameters, Phys. Rev. B **75**, 115104 (2007).

[4] J. D. Jackson, *Classical Electrodynamics* (Wiley, New York, 1998).

[5] M. G. Silveirinha, Generalized Lorentz-Lorenz formulas for microstructured materials, Phys. Rev. B **76**, 245117 (2007).

[6] A. Alù, First-principles homogenization theory for periodic metamaterials, Phys. Rev. B **84**, 075153 (2011).

[7] G. V. Eleftheriades and K. G. Balmain, Eds., *Negative-Refraction Metamaterials*, 5th ed. (Wiley, Hoboken, NJ, 2005).

[8] V. Ponsinet, A. Aradian, P. Barois, and S. Ravaine, in *Self-Assembly and Nanochemistry Techniques Towards the Fabrication of Metamaterials, in Applications of Metamaterials*, edited by F. Capolino (CRC, Boca Raton, FL, 2009), Chap. 32.

[9] A. Ahmadi and H. Mosallaei, Physical configuration and performance modeling of all-dielectric metamaterials, Phys. Rev. B **77**, 045104 (2008).

[10] I. Vendik, O. Vendik, and M. Odit, Isotropic artificial media with simultaneously negative permittivity and permeability, Microw. Opt. Technol. Lett. **48**, 12 (2006).

[11] I. Vendik, M. Odit, and D. Kozlov, 3D metamaterial based on a regular array of resonant dielectric inclusions, Radioengineering **18**, 111 (2009).

[12] L. Jylhä, I. Kolmakov, S. Maslovski, and S. Tretyakov, Modeling of isotropic backward-wave materials composed of resonant spheres, J. Appl. Phys. **99**, 043102 (2006).

[13] C. L. Holloway, E. F. Kuester, J. Baker-Jarvis, and P. Kabos, A double negative (DNG) composite medium composed of magnetodielectric spherical particles embedded in a matrix, IEEE Trans. Antennas Propagat. **51**, 2596 (2003).

[14] V. Yannopapas and A. Moroz, Negative refractive index metamaterials from inherently non-magnetic materials for deep infrared to terahertz frequencies, J. Phys.: Condens. Matter **17**, 3717 (2005).

[15] L. Lewin, The electrical constants of a material loaded with spherical particles, J. Inst. Electr. Eng. **94**, 65 (1947).

[16] A. Sihvola, *Electromagnetic Mixing Formulas and Applications*, IEE Electromagnetic Waves Series 47 (Stevenage, Herts, UK, 1999).

[17] R. A.Shore and A. D. Yaghjian, Traveling waves on three-dimensional periodic arrays of two different alternating magnetodielectric spheres, IEEE Trans. Antennas Propagat **57**, 3077 (2009).

[18] S. Ghadarghadr and H. Mosallaei, Dispersion diagram characteristics of periodic array of dielectric and magnetic materials based spheres, IEEE Trans. Antennas Propagat **57**, 149 (2009).

[19] R. A. Shore and A. D. Yaghjian, Traveling waves on two- and three-dimensional periodic arrays of lossless scatterers, Radio Sci. **42**, RS6S21 (2007).

[20] A. Alù, Restoring the physical meaning of metamaterial constitutive parameters, Phys. Rev. B **83**, 081102(R) (2011).

[21] A. Alù, A. Salandrino, and N. Engheta, Negative effective permeability and left-handed materials at optical frequencies, Opt. Express **14**, 1557 (2006).

[22] A. Vallecchi, M. Albani, and F. Capolino, Collective electric and magnetic plasmonic resonances in spherical nanoclusters, Opt. Express **19**, 2754 (2011).

[23] C. Fietz and G. Shvets, Current-driven metamaterial homogenization, Physica B **405**, 2930 (2010).

[24] M. G. Silveirinha, Poynting vector, heating rate, and stored energy in structured materials: A first-principles derivation, Phys. Rev. B **80**, 235120 (2009).

[25] V. M. Agranovich and S. Ginzburg, *Crystal Optics with Spatial Dispersion, and Excitons*, 2nd ed. (Springer, Berlin, 1984).

[26] A. Alù, A. D. Yaghjian, R. A. Shore, and M. G. Silveirinha, Causality relations in the homogenization of metamaterials, Phys. Rev. B, **84**, 054305 (2011).

[27] J. T. Costa, M. G. Silveirinha, and A. Alù, Poynting vector in negative-index metamaterials, Phys. Rev. B, **83**, 165120 (2011).

[28] C. Fietz and Costas M. Soukoulis, Scattering matrix of the boundary of a nonlocal metamaterial, Phys. Rev. B **86**, 085146 (2012).

[29] C. F. Bohren and D. R. Huffman, *Absorption and Scattering of Light by Small Particles* (Wiley, New York, 1983).

[30] X.-X. Liu and A. Alù, Generalized retrieval method for metamaterial constitutive parameters based on a physically driven homogenization approach, Phys. Rev B **87**, 235136 (2013).

[31] O. Breinbjerg, Properties of Floquet-Bloch space harmonics in 1D periodic magneto-dielectric structures, *International Conference on Electromagnetics in Advanced Applications (ICEAA)* (IEEE, Piscataway, 2012).